ARMY RESEARCH LABORATORY

ARL

Predictions of a Supersonic Jet-in-Crossflow: Comparisons Among CFD Solvers and with Experiment

by James DeSpirito, Kevin D Kennedy, Clark D Mikkelsen, and Ross A Chaplin

ARL-RP-0505   **September 2014**

NOTICES

Disclaimers

The findings in this report are not to be construed as an official Department of the Army position unless so designated by other authorized documents.

Citation of manufacturer's or trade names does not constitute an official endorsement or approval of the use thereof.

Destroy this report when it is no longer needed. Do not return it to the originator.

Army Research Laboratory
Aberdeen Proving Ground, MD 21005-5066

Predictions of a Supersonic Jet-in-Crossflow: Comparisons Among CFD Solvers and with Experiment

James DeSpirito
Weapons and Materials Research Directorate, ARL

Kevin D Kennedy, Clark D Mikkelsen
US Army Aviation and Missile, Research, Development and Engineering Center

Ross A Chaplin
Defence Science and Technology Laboratory

REPORT DOCUMENTATION PAGE		*Form Approved* *OMB No. 0704-0188*

Public reporting burden for this collection of information is estimated to average 1 hour per response, including the time for reviewing instructions, searching existing data sources, gathering and maintaining the data needed, and completing and reviewing the collection information. Send comments regarding this burden estimate or any other aspect of this collection of information, including suggestions for reducing the burden, to Department of Defense, Washington Headquarters Services, Directorate for Information Operations and Reports (0704-0188), 1215 Jefferson Davis Highway, Suite 1204, Arlington, VA 22202-4302. Respondents should be aware that notwithstanding any other provision of law, no person shall be subject to any penalty for failing to comply with a collection of information if it does not display a currently valid OMB control number.
PLEASE DO NOT RETURN YOUR FORM TO THE ABOVE ADDRESS.

1. REPORT DATE *(DD-MM-YYYY)*	2. REPORT TYPE	3. DATES COVERED (From - To)
September 2014	Final	January 2011–May 2014

4. TITLE AND SUBTITLE	5a. CONTRACT NUMBER
Predictions of a Supersonic Jet-in-Crossflow: Comparisons Among CFD Solvers and with Experiment	
	5b. GRANT NUMBER
	5c. PROGRAM ELEMENT NUMBER

6. AUTHOR(S)	5d. PROJECT NUMBER
James DeSpirito, Kevin D Kennedy, Clark D Mikkelsen, and Ross A Chaplin	AH80
	5e. TASK NUMBER
	5f. WORK UNIT NUMBER

7. PERFORMING ORGANIZATION NAME(S) AND ADDRESS(ES)	8. PERFORMING ORGANIZATION REPORT NUMBER
U.S. Army Research Laboratory ATTN: RDRL-WML-E Aberdeen Proving Ground, MD 21005-5066	ARL-RP-0505

9. SPONSORING/MONITORING AGENCY NAME(S) AND ADDRESS(ES)	10. SPONSOR/MONITOR'S ACRONYM(S)
	11. SPONSOR/MONITOR'S REPORT NUMBER(S)

12. DISTRIBUTION/AVAILABILITY STATEMENT

Approved for public release; distribution is unlimited.

13. SUPPLEMENTARY NOTES

Reprinted from the 32nd AIAA Applied Aerodynamics Conference 2014; 2014 Jun 16–20; Atlanta, GA.
Red Hook (NY): Curran Associates, Inc.; 2014. p. 2433–2458.

14. ABSTRACT

A supersonic jet interaction flowfield with pressure ratios of 2.8–16.7 exhausting into subsonic and transonic crossflows (Mach 0.5–0.8) was simulated using computational fluid dynamics and compared to experimental particle image velocimetry data. Three independent studies using different Reynolds-averaged Navier-Stokes flow solvers and a variety of turbulence models were used to assess the accuracy level of the predicted downstream flow physics of the jet interaction problem. Evaluation of the prediction of the downstream flow structure was made via comparisons of the three components of velcocity and turbulent kinetic energy. In general, the predicted jet interaction flowfield was highly sensitive to the turbulence model used, with performance of the turbulence model being dependent on the flow solver, and relatively insensitive to crossflow Mach number in the range investigated.

15. SUBJECT TERMS

lateral jet, computational fluid dynamics, aerodynamics

16. SECURITY CLASSIFICATION OF:			17. LIMITATION OF ABSTRACT	18. NUMBER OF PAGES	19a. NAME OF RESPONSIBLE PERSON James DeSpirito
a. REPORT	b. ABSTRACT	c. THIS PAGE	UU	32	19b. TELEPHONE NUMBER *(Include area code)* 410-306-0778
Unclassified	Unclassified	Unclassified			

Standard Form 298 (Rev. 8/98)
Prescribed by ANSI Std. Z39.18

Predictions of a Supersonic Jet-in-Crossflow: Comparisons Among CFD Solvers and with Experiment

James DeSpirito[*]

U.S. Army Research Laboratory, Aberdeen Proving Ground, Maryland 21005

Kevin D. Kennedy[†] and Clark D. Mikkelsen[‡]

U.S. Army Aviation & Missile, Research, Development & Engineering Center, Redstone Arsenal, AL 35898

and

Ross A. Chaplin[§]

Defence Science and Technology Laboratory, Fareham, Hampshire, PO17 6AD, UK

A supersonic jet interaction flowfield with pressure ratios of 2.8–16.7 exhausting into subsonic and transonic crossflows (Mach 0.5–0.8) was simulated using computational fluid dynamics and compared to experimental particle image velocimetry data. Three independent studies using different Reynolds-averaged Navier-Stokes flow solvers and a variety of turbulence models were used to assess the accuracy level of the predicted downsteam flow physics of the jet interaction problem. Evaluation of the prediction of the downstream flow structure was made via comparisons of the three components of velcocity and turbulent kinetic energy. In general, the predicted jet interaction flowfield was highly sensitive to the turbulence model used, with performance of the turbulence model being dependent on the flow solver, and relatively insensitive to crossflow Mach number in the range investigated.

Nomenclature

CFD   = computational fluid dynamics
CVP   = counter-rotating vortex pair
C_p = pressure coefficient
d = jet nozzle exit diameter, mm
J = jet-to-freestream dynamic pressure ratio
M = Mach number
p = pressure, Pa
PIV   = particle image velocimitry
q = dynamic pressure, Pa
T = temperature, K
TKE   = turbulent kinetic energy
u = streamwise component of velocity, m/s
U = resultant velocity, m/s
$U(x)$ = resultant velocity at specified x-location, m/s
v = vertical (ARL, AMRDEC) or lateral (DSTL) component of velocity, m/s
w = lateral (ARL, AMRDEC) or vertical (DSTL) component of velocity, m/s
x = streamwise distance from jet nozzle centerline, positive aft, m
y = distance from tunnel wall containing jet nozzle (ARL, AMRDEC) or lateral distance from tunnel

---

[*] Aerospace Engineer, Weapons & Materials Resarch Directorate, RDRL-WML-E, AIAA Associate Fellow.

[†] Aerospace Engineer, System Simulation & Development Directorate, RDMR-SSM-A.

[‡] Aerospace Engineer, System Simulation & Development Directorate, RDMR-SSM-A, AIAA Senior Member.

[§] Aerodynamicist, Air & Weapons Systems, PO17 6AD, UK, AIAA Member.

centerline (DSTL), m
y^+ = nondimensional turbulent boundary-layer coordinate
z = lateral distance from tunnel centerline (ARL, AMRDEC) or distance from tunnel wall containing jet nozzle (DSTL), m

Subscripts
j = jet
∞ = freestream conditions
0 = stagnation conditions

I. Introduction

JET-interaction thrusters provide a unique method for missile aerodynamic control with flexibility for control tailoring beyond that provided by traditional aerodynamic control surfaces. The resulting aerodynamic response to these thrusters, however, may be complex, since the interaction of the jet flowfield will couple with the external missile flowfield. Computational fluid dynamics (CFD) modeling provides a tool to predict a priori these jet interactions but validation is essential. Hence, opportunities are sought to compare CFD predictions for jet interaction (JI) flowfields with high quality, non-intrusive measurements.

Previous experimental research in this area has focused on two main applications: where a jet is housed in a flat plate,[1,2] such as the sidewall of a wind tunnel; or where a jet, or combination of jets, are integrated into a generic weapon configuration.[3,4] Many of the experimental databases used to validate computational tools to date have been limited to surface measurements such as pressure distributions[3] and oil flows.[2] However, there is a need to understand the off-surface flow physics and also the ability, or limitations, of modern computational techniques to predict the JI flowfield and the flow structures convected downstream. Thus, the experimental data set published by Beresh et al.[5–8] was chosen as a validation case.

The current research was completed as part of The Technical Cooperation Program[9] (TTCP) KTa 2-30-10 collaborative research activity on "Reaction Control Jets for Weapons" led by the U.S. Army Research Laboratory (ARL). The goal of the research activity was to asses the ability to use CFD to predict the complex flow physics associated with supersonic lateral jets injecting into subsonic through supersonic crossflows. Three independent numerical investigations of a supersonic lateral jet ejecting into subsonic and transonic crossflows over a flat plate were undertaken as part of this research activity—by investigators at the U.S. Army Aviation & Missile Research, Development & Engineering Center (AMRDEC),[10] the Defence Science and Technology Laboratory (DSTL)[11] in the United Kingdom, and ARL. The aim of this paper is to directly compare the results from the three independent investigations to each other and to the experimental validation data. The established experimental data set with high-fidelity flowfield measurements published by Beresh et al.[5–8] is used as the validation case and the effect of turbulence modeling, jet pressure ratio, and freestream Mach number are investigated.

II. Methodology

A. Experimental Set-Up and Measurement Description

The measurements reported in this paper were conducted in the Sandia National Laboratories Trisonic Wind Tunnel (TWT).[5–8] This facility uses heated air as the working fluid in a blowdown-to-atmosphere arrangement. The rectangular working section (see Fig. 1) is 305 mm x 305 mm (12 in. x 12 in.) and resides immediately downstream of the area reducing axisymmetric-to-rectangular transition inflow hardware. For the current experiments, the porous walls of the test section were replaced with solid walls. As stated in Beresh et al.,[5] this both served as the flat plate from which the jet would issue and provided tractable boundary conditions for comparison with numerical simulations. The sold-walled test section did limit the Mach number range of the TWT to below normal levels. In all cases, the nominal working section static pressure measured on the wind tunnel sidewalls remained at $p_\infty = 101$ kPa. Data was taken at freestream Mach numbers from $0.5 \leq M_\infty \leq 0.8$. At the primary freestream Mach number of $M_\infty = 0.8$, the wind tunnel total pressure and temperature were $p_0 = 154$ kPa and $T_0 = 324$ K, respectively, and resulted in a freestream unit Reynolds Number of Re/m = 20 x 10^6.

The transverse supersonic jet was produced using a converging-diverging nozzle with a design Mach number of 3.73, a conical expansion section half-angle of 15 degrees, and an exit diameter of 9.53 mm. The nozzle was mounted along the tunnel lateral centerline in the upper wall of the subsonic test section and fed from unheated bottled nitrogen through a settling chamber at stagnation conditions of up to $p_{0j} = 14$ MPa and approximately $T_{0j} = 300$ K. In this paper, results are discussed for several jet stagnation pressure conditions ($1.36 \leq p_{0j} \leq 8.14$ MPa),

2
American Institute of Aeronautics and Astronautics

which correspond to jet-to-freestream dynamic pressure ratios of $2.8 \leq J \leq 16.7$. Most data was taken at $M_\infty = 0.8$ and $J = 10.2$, which is labeled the "priority case" in the following sections.

The primary measurements taken were Particle Image Velocimetry (PIV) fields downstream of the initial jet interaction flowfield. In addition, wall static pressure measurements on the tunnel sidewall were taken. Two dimensional velocity measurements were taken on a measurement plane aligned with the freestream flow on the tunnel centerline. Stereoscopic 3D velocity measurements were taken on a crossplane at $x/d_j = 33.8$ downstream of the nozzle, where x is defined as the streamwise distance downstream of the jet nozzle centerline. Only the wind tunnel freestream flow was seeded (the jet was not), however the authors claim the measurement planes were far enough downstream that the seeding was fully mixed into the interaction flowfield due to turbulent mixing. Full details of the PIV measurements and the post-processing approach used are given in Ref. 12.

Figure 1 is an illustration of the test section taken from Beresh et al.[8] and shows the location of the jet installed in the tunnel top wall as well as the two PIV measurement planes. The flat sidewalls of the subsonic test section offered access for the PIV data collection. A sidewall window was located flush with the lower wall for viewing downstream interactions. A window was also located along the top wall of the test section to accommodate a PIV laser sheet. For the PIV data collection, the TWT was seeded by a thermal smoke generator that produces particles typically 0.2-0.3 μm in diameter from a mineral oil base. Additionally, two sidewall pressure taps were added for measuring the test section static pressure and to determine the nominal freestream Mach number.

Additional details of the PIV setup and measurements, and wind tunnel and model construction, are given in References 5–8. Although the jet nozzle was physically located in the upper wall of the tunnel, the PIV data was oriented with the nozzle at y = 0. Hence, the comparisons with CFD results are presented with nozzle on the bottom wall and the jet plume penetrating the flowfield with y > 0. It should be noted that a different orientation scheme was used in the DSTL study, with z defined as the distance from the tunnel top wall (positive downward) and y the lateral distance from the tunnel centerline.
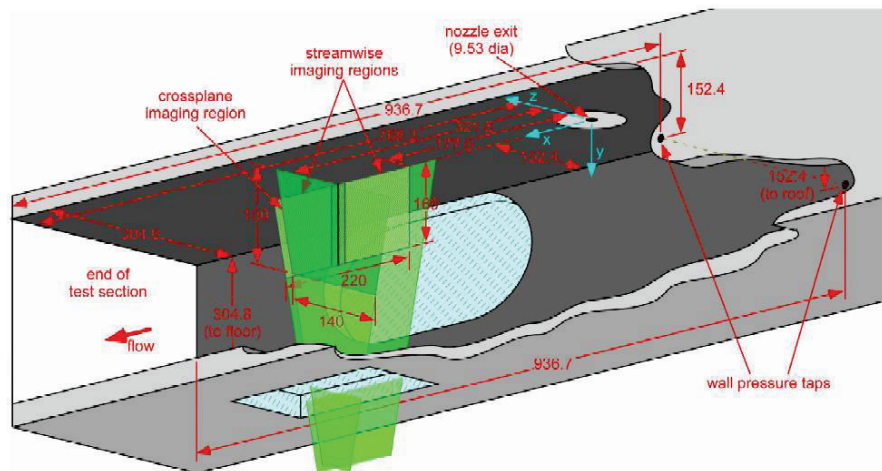

Figure 1. Wind tunnel schematic and measurement locations, from Beresh et al.[8] Flow from right to left.

B. Computational Approach

A solid model and additional information on the Sandia TWT, including the jet nozzle dimentions and the experimental data from Refs 5–8 was provided to the authors by Dr. Beresh of Sandia National Laboratories.[*] This information was used by the authors to generate the computational domain and compare our predictions with the experimental data in Section III.

1. AMRDEC

The computational domain and grid zonal structure is shown in Fig. 2. A representation of the complete wind tunnel nozzle section and test section was included in the computational model. The computational domain was rotated 180° from the orientation in the experimental setup so that the jet nozzle is on the wind tunnel floor. The AMRDEC grid was generated using GRIDGEN[13] version 15.17 as a combination of *H*-type and *C*-type grids. For clarity, only the edges of each block are shown. The nozzle flow and resulting plume were made up of a center core

---

[*] Private communication, Beresh, S. J. and Arunajatesan, S., August 2011.

H-type grid surrounded by a *C*-type grid. This formulation was used to prevent a nozzle centerline "pole" and to resolve the nozzle wall boundary layer. Additionally, an *H*-type grid was used upstream of the jet. Around the downstream jet, the *H/C/C/H*-type grid conforms and follows the plume. This scheme allows for an optimal cell clustering around the jet and barrel shock. In addition, the boundary layer cells closest to the tunnel and nozzle surface had a first cell height of 1.0 x 10^{-6} m that resulted in a y^+ of 1.0 or less using a fully resolved So-Zhang-Speziale wall model.[14] A one-dimensional monotonic rational quadratic spline (MRQS) function was used to space all grid points. The final grid of 17.3 million points was used for all of the CFD calculations.

For the modeled computations, the nozzle exit plane was centered at the origin. The origin location and coordinate system are defined by the red axis in Fig. 2 with the *x*-axis defining the downstream direction and the *y*-axis defining the normal distance from the tunnel floor. All calculations and measurements are referenced to this location.

Fluid dynamic boundary conditions for the calculations were as follows, based on published flow characteristics of the TWT.[8] The tunnel air and nitrogen jet gases were modeled as perfect gases ($\gamma = 1.4$). The tunnel and nozzle walls were defined as solid surfaces with adiabatic walls and no-slip conditions. The jet nozzle inflow conditions of total pressure was set to 1.36, 2.76, 4.97, and 8.14 MPa to give jet-to-freestream dynamic pressure ratios of 2.8, 5.6, 10.2, and 16.7, respectively. The total temperature was set to 301.5 K. The subsonic wind tunnel inflow conditions were set with a total pressure of 0.154 MPa and total temperature of 326.5 K to give a Mach 0.8 crossflow in the test section. Subsonic extrapolation procedures were used at the outflow boundary with a backpressure of 94.5 kPa. The initial background levels of turbulence were set to zero.

For a subsonic outflow, the CFD exit conditions are set by the backpressure, which unfortunately was not measured in the experiments. As a means to work around this shortcoming, the backpressure of 94.5 kPa was established through a numerical iteration process to match (at one *x*, *y*, *z* location) the measured PIV freestream *u*-velocity of 279.6 m/s at the farthest downstream measurement point with the results of the fluid dynamic computations. Both the measurement and computations were for a jet off tunnel condition. This same backpressure was then used for the jet on calculations.
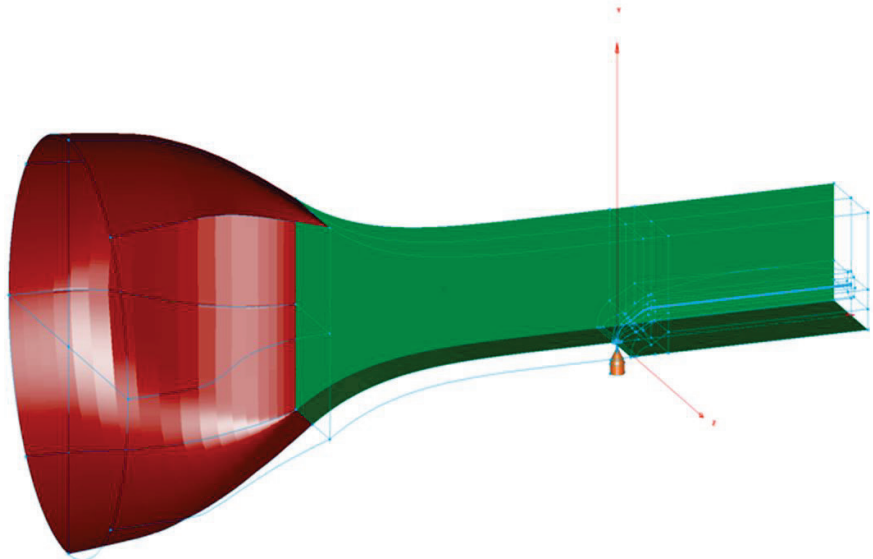

Figure 2. AMRDEC computational domain and grid zonal structure.

The AMRDEC CFD model includes the full Navier-Stokes (FNS) equation set providing an aero-thermo-chemical plume / airframe predictions for unsteady-flows.[15–17] The CFD code numerics include 1D/2D/Axi/3D finite volume discretization with an implicit, higher-order upwind (Roe/TVD) formulation that is 2nd order for the Reynolds-average Navier-Stokes (RANS) formulation and 5th order for the Large-Eddy Simulation (LES) formulation. The turbulence model includes a *k*-ε (rke)formulation with compressibility/vortical upgrades over standard models and includes several low-Re, near-wall formulations. A variable, one/two-equation Prandtl number/Schmidt model has been recently added. All equations are solved either fully implicitly or loosely coupled. This code solves the discretized integral form of the time-dependent FNS equations over a structured contiguous/non-contiguous multigrid. The code is written in FORTRAN 90 with MPI extensions. For this study, this CFD model was executed on a 320-node (640 CPUs) Apple G5 cluster with an IBM XLF compiler.

4

American Institute of Aeronautics and Astronautics

2. DSTL

Two wind tunnel arrangements were modeled: the first without the jet, which simulated the "jet-off" experiment and the second with the jet nozzle and plenum represented. A rectangular prism-shaped computational domain was used that modeled one half of the wind tunnel working section, using a symmetry plane on the tunnel lateral centerline. In the DSTL simulations the wind tunnel settling chamber and nozzle were not modeled and an illustration of the jet-on domain is shown in Fig. 3a.

In all cases, the wind tunnel walls were modeled as no-slip boundaries. The symmetry plane was modeled with a symmetry boundary condition. The tunnel inflow and outflow boundaries were specified as modified Riemann invariants conditions at the freestream flow conditions. The computational inlet is a planar face and its location was varied until a satisfactory boundary-layer was predicted for the jet-off case. Moreover, the domain outlet pressure was varied until a satisfactory wall pressure distribution was observed. The nozzle walls were modeled as no-slip boundaries and the nozzle stagnation conditions were applied to the plenum inlet face as shown in Fig. 3b.

An unstructured grid approach was used where tetrahedral cells covered most of the domain and prismatic cells were used in the boundary-layer. Local grid refinement was used near to the wind tunnel walls to resolve the boundary layer and ensure an average non-dimensional y^+ of less than one with a clustering ratio of approximately 1.2 over the boundary-layer thickness. The grid was further resolved in the region around the jet nozzle and also in the tunnel freestream where the PIV measurement planes were located as shown in Figs. 4a and 4b. Although no quantitative grid convergence study was performed, the density of the flowfield refinement regions were improved over several iterations until suitable predicted results were observed. The no-jet grid is not shown here but it used the same flowfield grid refinement. The total grid size for the no-jet case was approximately 24 M cells and for the jet-on case was approximately 25.5 M cells.


(a)   (b)
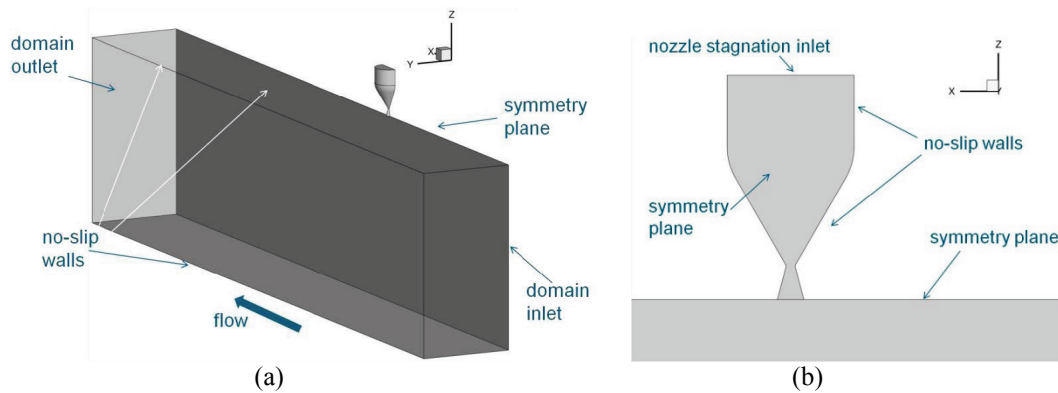
Figure. 3 DSTL computational domain showing (a) half of wind tunnel with a symmetry plane and (b) nozzle and plenum region.


(a)   (b)
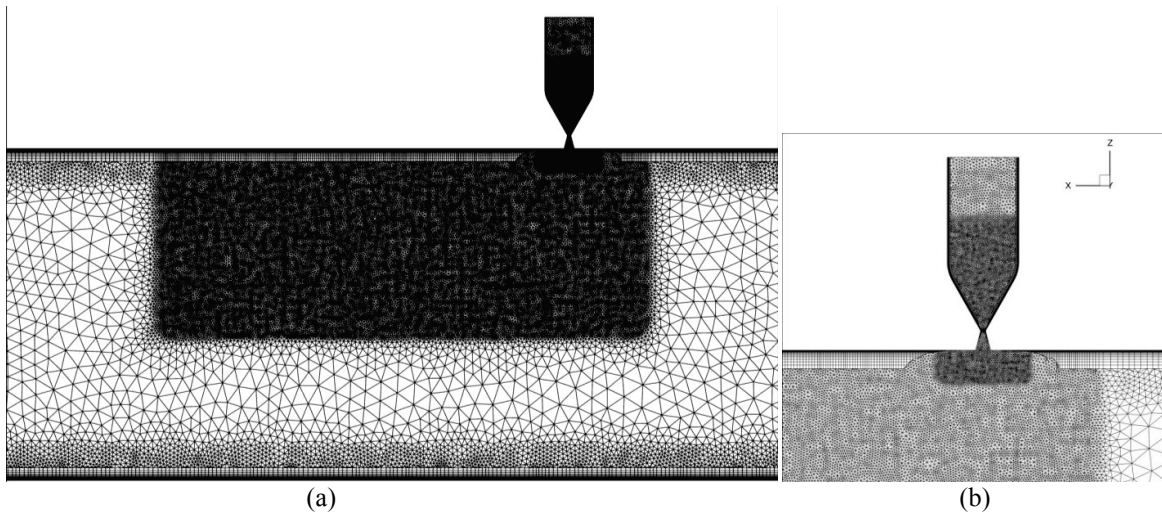
Figure. 4. DSTL unstructured mesh on computational symmetry plane (a) showing grid refinement regions and (b) close-up of mesh near the jet nozzle. Flow from right to left.

5

American Institute of Aeronautics and Astronautics

All computational predictions were conducted using the Cobalt[18] flow solver. This is an unstructured, implicit solver based on a finite volume formulation; further details are reported by Strang et al.[19] Steady-state, RANS predictions were performed using the one-equation Spalart-Allmaras (SA),[20] the SA model with rotation/curvature correction (SARC),[21] and the two-equation k-ω (KW),[22] and k-ω SST (SST)[23,24] models. All computational predictions were computed with 2nd order spatial accuracy and 1st order temporal accuracy. The jet working fluid in the computations was air rather than nitrogen as used in the experiment. A summary of the computational matrix is given in Table 1. All computations demonstrated suitable levels of iterative convergence.

Table 1. DSTL computational matrix and flow conditions.

M_∞	J	$^*p_0$ [kPa]	p_∞ [kPa]	T_0 [K]	M_j	$^\dagger p_{oj}$ [MPa]	T_{0j} [K]	Turbulence Model
0.8	–	145.6	95.5	324	–	–	–	SA, SARC, k-ω, SST
0.8	10.2	145.6	95.5	324	3.73	4.97	300	SA, SARC, k-ω, SST
0.8	16.7	145.6	95.5	324	3.73	8.14	300	SA
0.8	5.6	145.6	95.5	324	3.73	2.76	300	SA
0.8	2.8	145.6	95.5	324	3.73	1.36	300	SA
0.7	10.2	132.5	95.5	324	3.73	3.82	300	SA
0.6	10.2	121.8	95.5	324	3.73	2.79	300	SA
0.5	10.2	113.3	95.5	324	3.73	1.96	300	SA

*Slightly lower value than used in Ref. 5 to adjust for inflow boundary location.
†Corrected values for M_∞ = 0.5, 0.6, and 0.7; incorrect values were listed in Table 1 of Ref. 11.

3. ARL

The computational domain used in the ARL investigation is shown in Fig. 5. The computational domain, like that used by AMRDEC, was based on a solid model of the TWT supplied by Sandia and included the wind tunnel nozzle and test sections. Simulations were performed with both a half-domain with a symmetry plane representation and a full-domain representation. The latter was generated by mirroring the half-domain mesh. All solid walls were no-slip boundaries. The wind tunnel nozzle inlet and the jet nozzle plenum inlet were set at stagnation pressure and temperature conditions. The tunnel outlet was a simple back-pressure boundary condition.
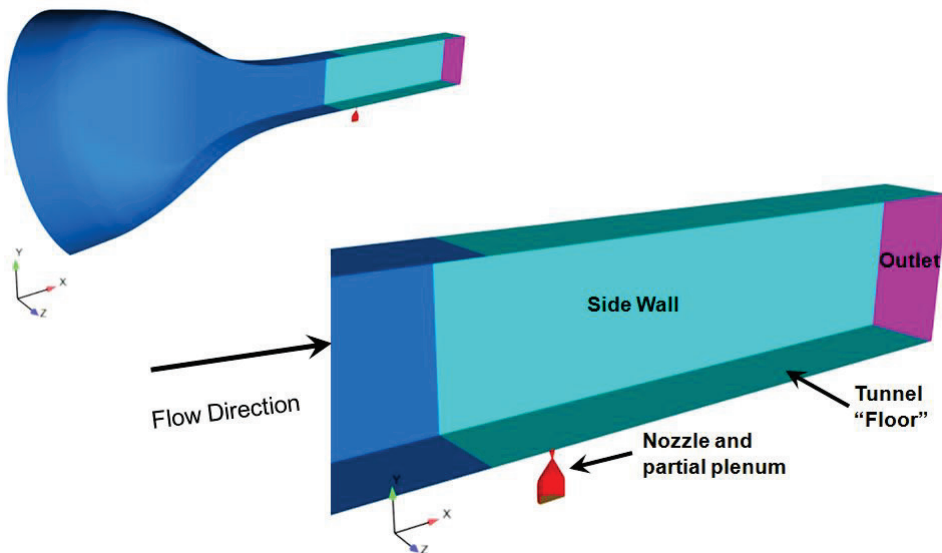

Figure 5. ARL computational domain.

The computational mesh was generated using the MIME[25] grid generator and is shown in Fig. 6. One-half of the physical domain was meshed using quad-dominant cells on the wind tunnel walls, ceiling, and floor and triangular cells on the jet nozzle and plenum walls. Prism layers ($y^+ \leq 1$, first cell layer $\Delta y = 3 \times 10^{-6}$ m) were generated from

each solid wall giving rectangular prismatic and tetrahedral cells in the interior volume and quadrilateral and triangular cells on the fluid boundaries (wind tunnel inlet and outlet, the jet nozzle plenum, and the symmetry plane). This computational mesh was mirrored to generate a full-domain mesh when required.

A grid resolution investigation was performed to determine the baseline size of the no-jet mesh that was required. A series of mesh density boxes were then used to refine the mesh in the jet nozzle exit and downstream sections of the computational domain (the extent of these can be seen on the wind tunnel floor and symmetry plane in Fig. 6). A more detailed view of the mesh in the jet nozzle area is shown in Fig. 7, again showing several mesh density boxes used to refine the mesh in critical areas. There was no interface between the wind tunnel test section and the jet nozzle exit. The mesh size was 3.6 M cells for the half-domain, jet-off cases, and 14 M cells and 28 M cells for the half- and full-domain meshes, respectively, for the jet-on cases.
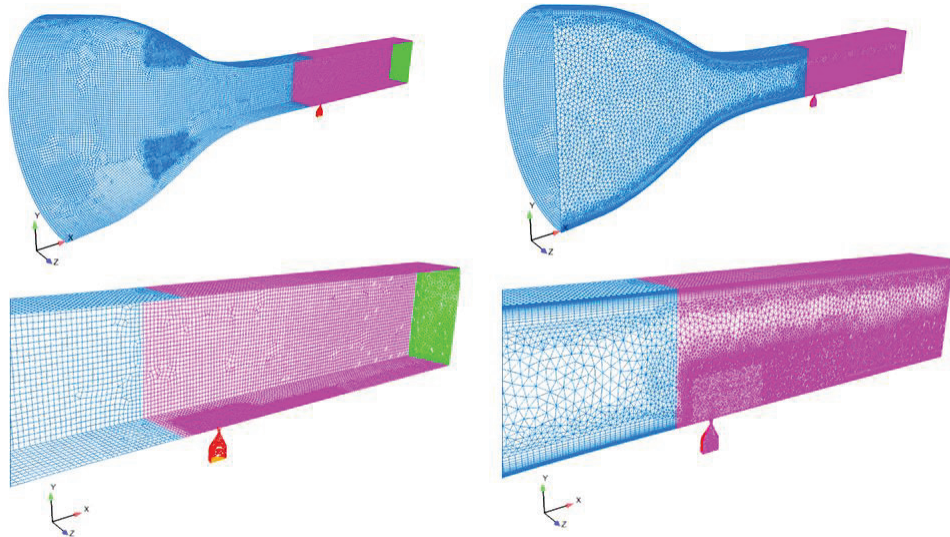
Figure 6. ARL computational mesh.
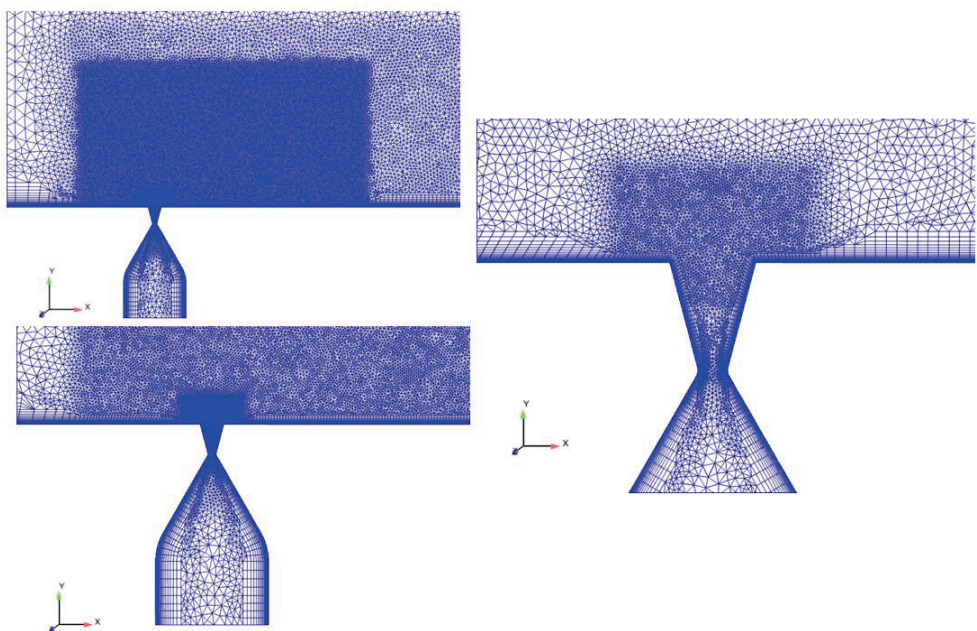
Figure 7. ARL geometry and mesh in jet nozzle area.

7

American Institute of Aeronautics and Astronautics

The data from Reference 8 were used to determine the wind tunnel boundary conditions required to match the following parameters as closely as possible to the experiment: the boundary layer thickness, freestream pressure, and core flow Mach number variation with *x*-distance. The ARL investigation considered the *J* = 10.2, Mach 0.8 crossflow case. The stagnation conditions at the wind tunnel inlet were p_0 = 154 kPa and T_0 = 325 K. The stagnation conditions at the nozzle plenum inlet were p_0 = 4.96 MPa and T_0 = 300 K. The value of the back pressure at the tunnel outlet was p_∞ = 94.5 kPa, which was estimated using the Fanno flow equations—based on the experimentally measured pressure in the test section—then adjusted further to match the experimental wind tunnel conditions.

The commercially available CFD[++] code,[26] version 11.1, was used in the ARL study. The 3-D, compressible, RANS equations are solved using a finite volume method. A point-implicit time integration scheme with local time-stepping, defined by the Courant-Friedrichs-Lewy (CFL) number, was used to advance the solution towards steady-state. The multigrid W-cycle method with a maximum of 4 cycles and a maximum of 20 grid levels was used to accelerate convergence. Implicit temporal smoothing was applied for increased stability. The inviscid flux function was a second-order, upwind scheme using a Harten-Lax-van Leer-Contact (HLLC) Riemann solver and a multi-dimensional Total-Variation-Diminishing (TVD) continuous flux limiter.

The choice of turbulence model is a key factor in the numerical modeling of complex flows such as this. CFD[++] has available a large set of standard turbulence models, four of which were investigated for their accuracy in prediction of the downstream JI flowfield. The models investigated in this study were the two-equation Menter's *k*-*ω* Shear Stress Transport (SST) model,[23] the cubic *k*-*ε* (cke) model,[27] and Goldberg's three-equation *k*-*ε*-*R* (keR) model.[28]

The mesh was partitioned with roughly 150 k cells per computational core using 96 cores for half-domain simulations and 192 cores for full-domain simulations. Simulations were performed on the SGI ICE X System (SPIRIT) located at the U.S. Air Force Research Laboratory DoD Supercomputing Resource Center (DSRC) at Wright-Patterson Air Force Base, OH, the Cray XE6 (GARNET) located at the U.S. Army Engineering Research and Development Center DSRC in Vicksburg, MS, and the IBM iDataPlex (PERSHING) and SGI Altix ICE 8200 (HAROLD) located at the U.S. ARL DSRC at Aberdeen Proving Ground, MD.

III. Results and Discussion

The results in this paper are presented in two parts: the validation of jet-off and jet-on predictions. First, in order to assess the capability of CFD to predict the wind tunnel flowfield without the jet interaction, a series of jet-off calculations were performed and compared to the measurements for a case where the jet nozzle exit was closed with a blanking piece in the experiment. Second, the effect of turbulence model, jet pressure ratio, and freestream Mach number on computational accuracy is presented and discussed for cases where the jet is on. Previous researchers[5–8] have presented a detailed description of the flow physics involved in the jet interaction for the cases discussed in this paper. Therefore, this will not be repeated here; instead this paper will focus on the ability, or limitations, of the CFD to predict the JI flowfield measured in the experiment.

A. Jet-Off Results

Before computing the jet-on cases, each investigator followed their own process to obtain the best match between their predicted wind tunnel flow conditions and those presented in Ref. 8. The primary metrics to determine the prediction accuracy were the boundary-layer velocity profiles on the wind tunnel centerline at x/d_j = 30.3 and the static pressure distributions on the tunnel side wall 16 jet diameters from the tunnel floor.

Figures 8a and 8b show the *u*-velocity and *u*-velocity deficit profiles, respectively, predicted by each organization. All three results are very good to excellent. The AMRDEC result is the closest to the experimental data, followed by the ARL prediction. The excellent AMRDEC result was only achieved after delaying the laminar-to-turbulent flow transition in the CFD model to a location 0.48 m upstream of the jet nozzle centerline. A transition model was not used in the ARL or DSTL simulations; the only parameter that was varied to achieve this level of agreement was the tunnel outflow boundary static pressure. The boundary layer velocity profiles are generally close to the measured data in terms of both the velocity profile and the maximum boundary-layer thickness, which ranged from 14.5–15.4 mm in the DSTL predictions, 14.3 mm in the AMRDEC predictions, and 13.2 mm in the ARL predictions. The boundary-layer thickness was 13.4 mm in the experiment.[8] The turbulence models used in the data presented in Fig. 8 are indicated; however, DSTL and ARL simulations showed the tunnel flow was insensitive to the specific turbulence model used.[11,29]

Figure 9 shows the comparison of measured and predicted static pressure distribution on the midpoint of the tunnel sidewall for the DSTL and ARL simulations. Both CFD simulations generally capture the reduction in

pressure due to the streamwise acceleration of the flow; however, there is a difference in the predicted gradient of the pressure distribution ($\delta p/\delta x$). The ARL simulation has a smaller difference in the pressure gradient and predicts the pressure better at the location that the velocity profiles are compared ($x/d_j = 30.3$). It is likely that ARL using simulations of the full tunnel, including the nozzle, leads to a better match.


(a) (b)
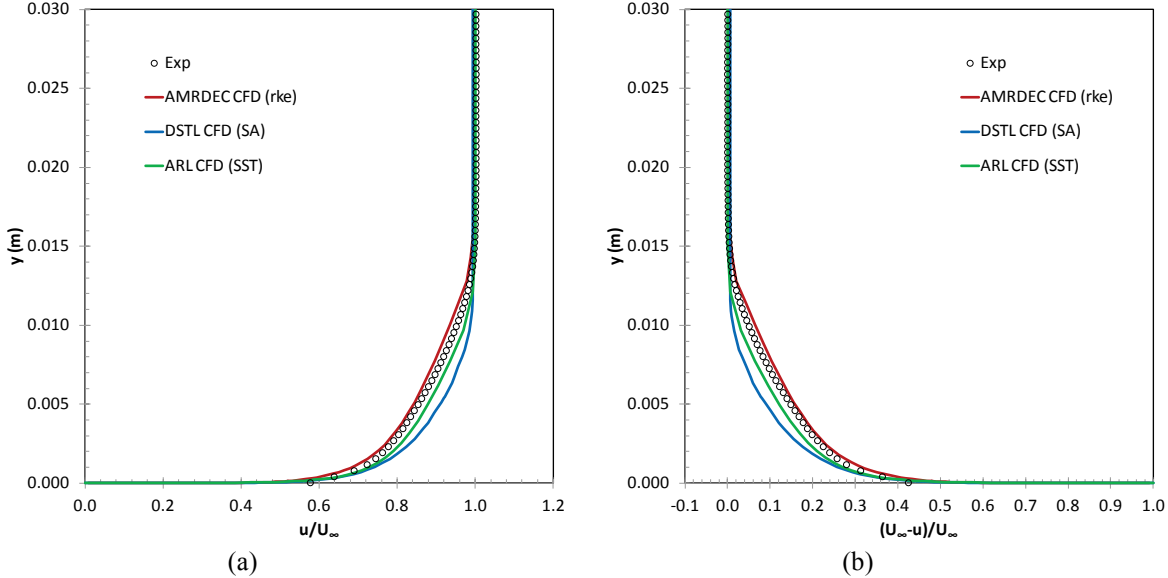
Figure 8. Measured and predicted jet-off boundary-layer (a) *u*-velocity and (b) *u*-velocity deficit profiles on the tunnel centerline at $x/d_j = 30.3$ and $M_\infty = 0.8$.
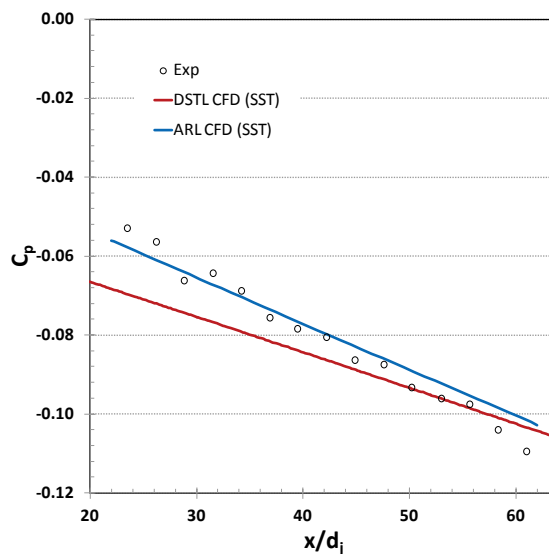
Figure 9. Measured and predicted static pressure distributions on the tunnel side walls for $M_\infty = 0.8$ for DSTL and ARL results at $y/d_j = 16$.

B. Jet-On Results

1. Priority case, $M_\infty = 0.8$, $J = 10.2$: Effects of turbulence model and solver prediction comparisons

The predictions of the jet-off wind tunnel flowfield showed little sensitivity to turbulence modeling, however, it was considered important to assess this sensitivity again for the jet-on cases due to the turbulent mixing involved in the interaction flowfield. DSTL and ARL performed a series of simulations to investigate the effect of turbulence model for the priority jet-on test case at $M_\infty = 0.8$ and $J = 10.2$. AMRDEC performed the priority jet-on test case for

American Institute of Aeronautics and Astronautics

only a single turbulence model, but performed a more in-depth analysis of the turbulent statistics and percent error differences between the predicted and measured data.

The measured[5] and DSTL predicted[11] streamwise velocity contours are shown in Fig. 10 and Fig. 11, respectively. DSTL computational predictions are presented in Fig. 11 for four different turbulence models: SA, SARC, k-ω and SST. The measured data region covers the streamwise PIV measurement plane where x is the distance downstream of the jet centerline and z (y in Ref. 5 and ARL simulations) is the distance from the wind tunnel top wall and is positive downward towards the centre of the tunnel. The streamwise velocity component (u) is non-dimensionalized by the nominal freestream velocity (U_∞). Previous researchers[5,7] reported the freestream velocity for this case as U_∞ = 286 m/s and this has been used to non-dimensionalize the measured data. However, for the DSTL and ARL predictions a value of U_∞ = 272 m/s is used, which is calculated from the isentropic relations at M_∞ = 0.8 and T_0 = 324 K. All results are plotted on the same non-dimensional scale to be consistent. It appears that the Sandia results were processed using the u-velocity from largest accelerated tunnel Mach number of 0.84, or 285.9 m/s, to normalize the flowfield (e.g., Table 1, Ref. 5). In the velocity profiles shown later, the u- and v-velocities are normalized by the maximum freestream velocity achieved at that profile location in the jet-off simulations, which ranged from U_∞ = 279.3 at x/d_j = 21.0 to U_∞ = 282.3 at x/d_j = 42.0.

The measured data in Figure 10 shows the normalized u-velocity contours. The deficit in the streamwise velocity component tracks the position of the jet plume core, as it impedes the oncoming crossflow. With increasing downstream position, the jet core strength reduces and its position is further from wall. The freestream velocity increases with increasing streamwise distance due to the blockage effect of the jet and boundary-layer. Figure 10 also shows the wake flow features close to the wall shown by regions where the local velocity is less than the freestream.
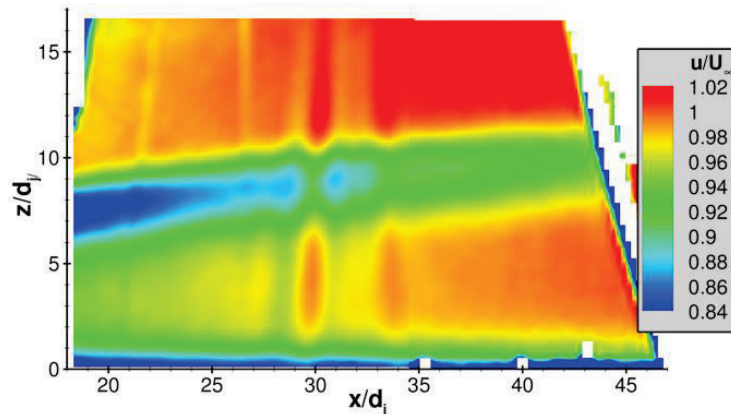
Figure 10. Experimental u-velocity contours on the tunnel centerline, M_∞ = 0.8, J = 10.2 (Beresh et al.[5]).

Overall, in Fig. 11a–d the qualitative flow features are captured by all of the different turbulence models. However, the k-ω and SST models overpredict the plume strength and position from the wall in Fig. 11c and Fig. 11d, respectively. The predicted size and extent of the jet plume for both the SA and SARC models are closer to the experiment than the k-ω and SST predictions. In both cases, the increasing freestream velocity with downstream distance is well predicted and so are the wake features between the jet and the wall. The additional wake feature in the SA prediction is not observed in the experiment. All in all, qualitatively the SA and SARC models provide the closest agreement with measured u-velocity data.

Figure 12a–c shows the ARL predicted streamwise velocity contours for the SST, cke, and keR models, respectively. From Fig. 12, it appears that qualitatively the cke and keR predictions provide a closer match to the experimental data (Fig. 10). However, later it will be shown that the predictions with the SST model actually provide a more accurate peak u-velocity deficit prediction, while all three models over predict the penetration of the jet into the crossflow. Similar turbulence model performance was observed when considering the vertical velocity (w-velocity in DSTL investigation, v-velocity in AMRDEC, ARL, and experiment investigations) component.[10,11,29]

The quantitative u-velocity deficit profiles are extracted at x/d_j = 21.0, 31.5, and 42.0 to further investigate the qualitative results. Figure 13 shows the DSTL predicted u-velocity deficit profiles on the tunnel centerline compared to the experimental data. The parameter $U_\infty(x)$ is the local freestream velocity at a given tunnel x-location and, as expected, all profiles collapse to zero velocity deficit far from the wall. The DSTL results show the two-equation turbulence models (k-ω and SST) perform poorly for this case. The peak velocity deficit, which is related

to the jet plume strength, is similar for the SA and SARC predictions and in both cases this is within the experimental uncertainty. The SARC prediction shows the plume trajectory to be closer to the wall than the measured data, whereas the SA prediction shows this to be further from the wall. The velocity deficit associated with the wake features close to the wall is observed and an additional feature is seen in the SA prediction at $z/d_j = 4$, which is not observed in the measured data. Overall, the SA prediction is marginally closer to the experiment than the SARC prediction over most of the profile and in the region below $z/d_j = 8$, the SA prediction is generally within the experimental uncertainty.

(a) (b)

(c) (d)
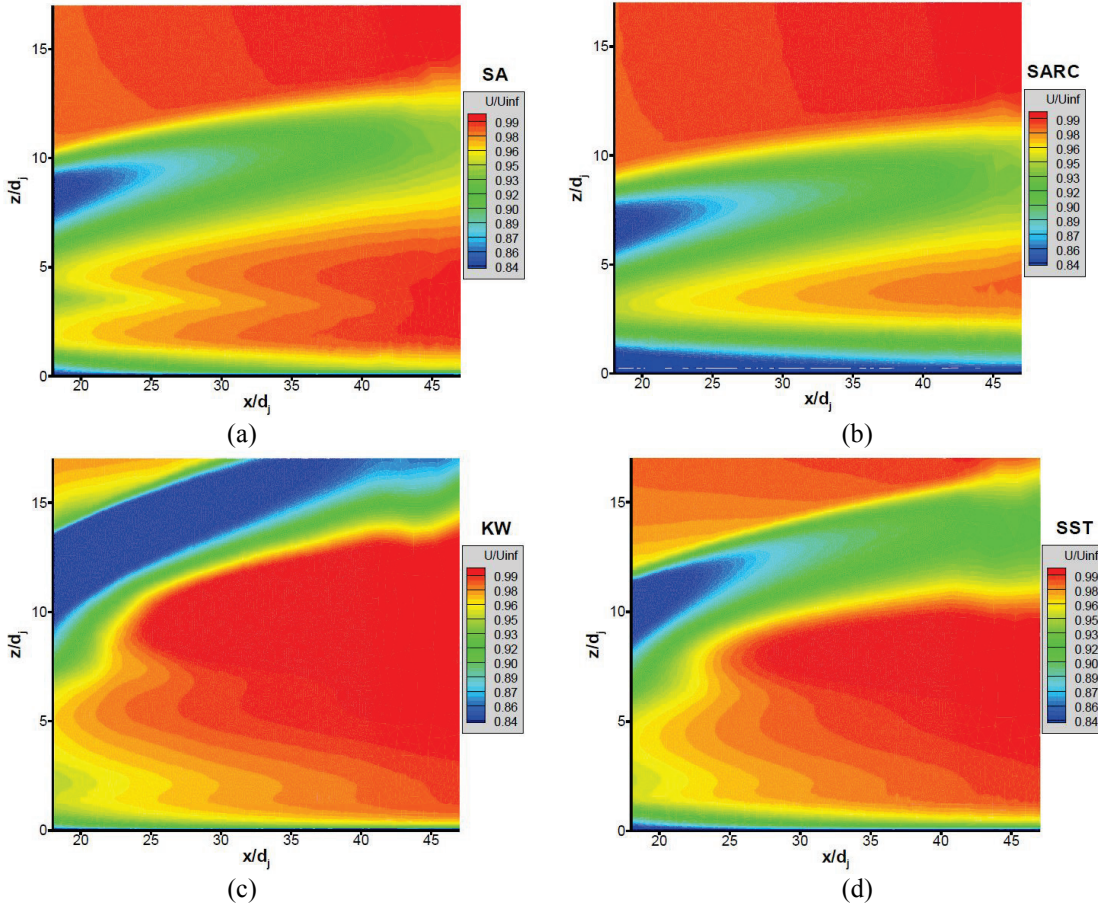
Figure 11. DSTL predicted *u*-velocity contours on tunnel centerline using (a) SA, (b) SARC, (c) *k-ω*, and (d) *k-ω* SST turbulence models, $M_\infty = 0.8$, $J = 10.2$.

(a) (b) (c)
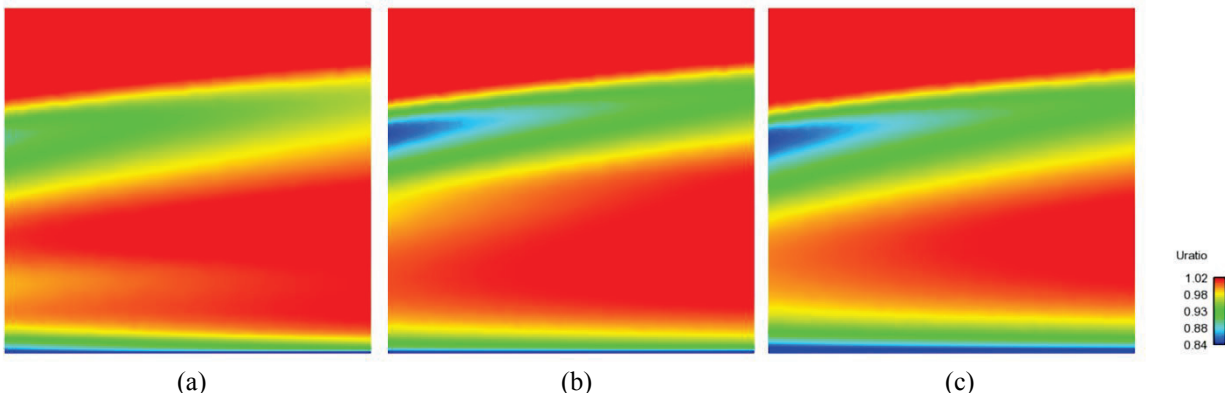
Figure 12. ARL predicted *u*-velocity contours on tunnel centerline using (a) SST, (b) cke, and (c) keR turbulence models, $M_\infty = 0.8$, $J = 10.2$.

11
American Institute of Aeronautics and Astronautics

Figure 14 shows the DSTL predicted vertical (*w)* velocity profiles on the tunnel centerline at different downstream locations. Figure 14 confirms that the k-ω and SST predictions significantly overpredict the peak *w*-velocity. As the position of the counter-rotating vortex pair (CVP) can be identified on the tunnel centerline by the maximum vertical (*w*) velocity, it is also observed that these two model also overpredict the penetration of the jet into the crossflow. The SARC model closely predicts the peak vertical velocity; however, there is a notable discrepancy close to wall. Overall, the SA prediction is closest to the measured data over most of the profile.
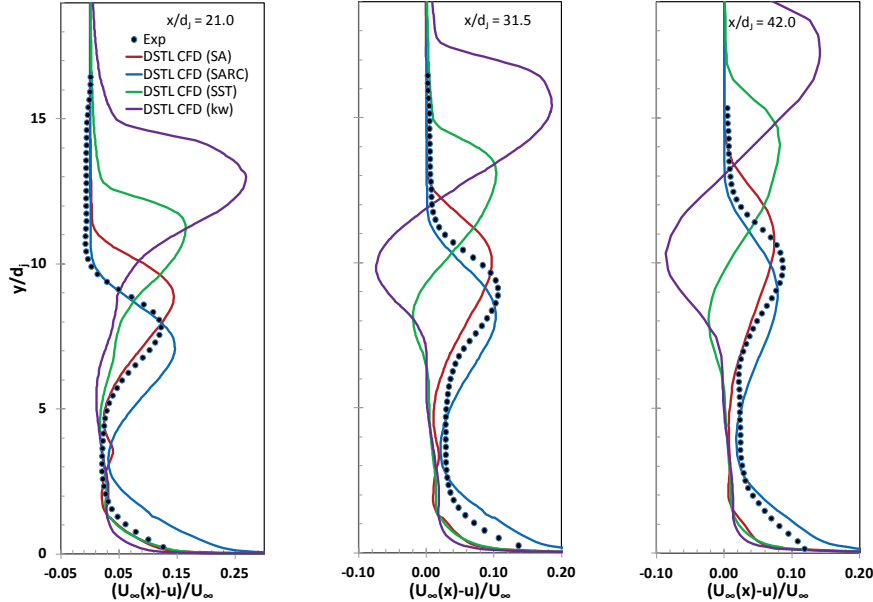
Figure 13. Measured and DSTL predicted *u*-velocity deficit profiles on the tunnel centerline at x/d_j = 21.0, 31.5, and 42.0, M_∞ = 0.8, J = 10.2.
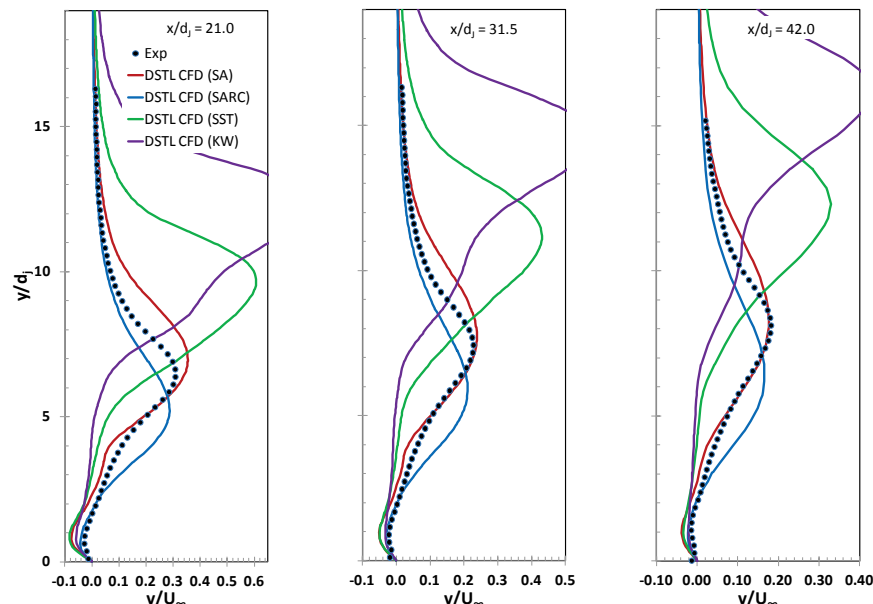
Figure 14. Measured and DSTL predicted *w*-velocity profiles on the tunnel centerline at x/d_j = 21.0, 31.5, and 42.0, M_∞ = 0.8, J = 10.2.

The ARL predicted *u*- and *v*-velocity profiles at downstream locations x/d_j = 21.0, 31.5, and 42.0 are shown in Fig. 15a and 15b, respectively. In this case, the peak *u*-velocity deficit (Fig. 15a) is predicted best with the SST

12

American Institute of Aeronautics and Astronautics

turbulence model, which provides the closest match in the peak velocity deficit. The predicted peak v-velocity and penetration distance (Fig. 15b) was similar for all three turbulence models. The data in Fig. 15 were for the half-domain CFD simulations. Comparison of ARL predicted velocity profiles using the half- and full-domain (mirrored mesh) meshes showed only small differences in the near-wall u-velocity profiles.[29]

(a)

(b)
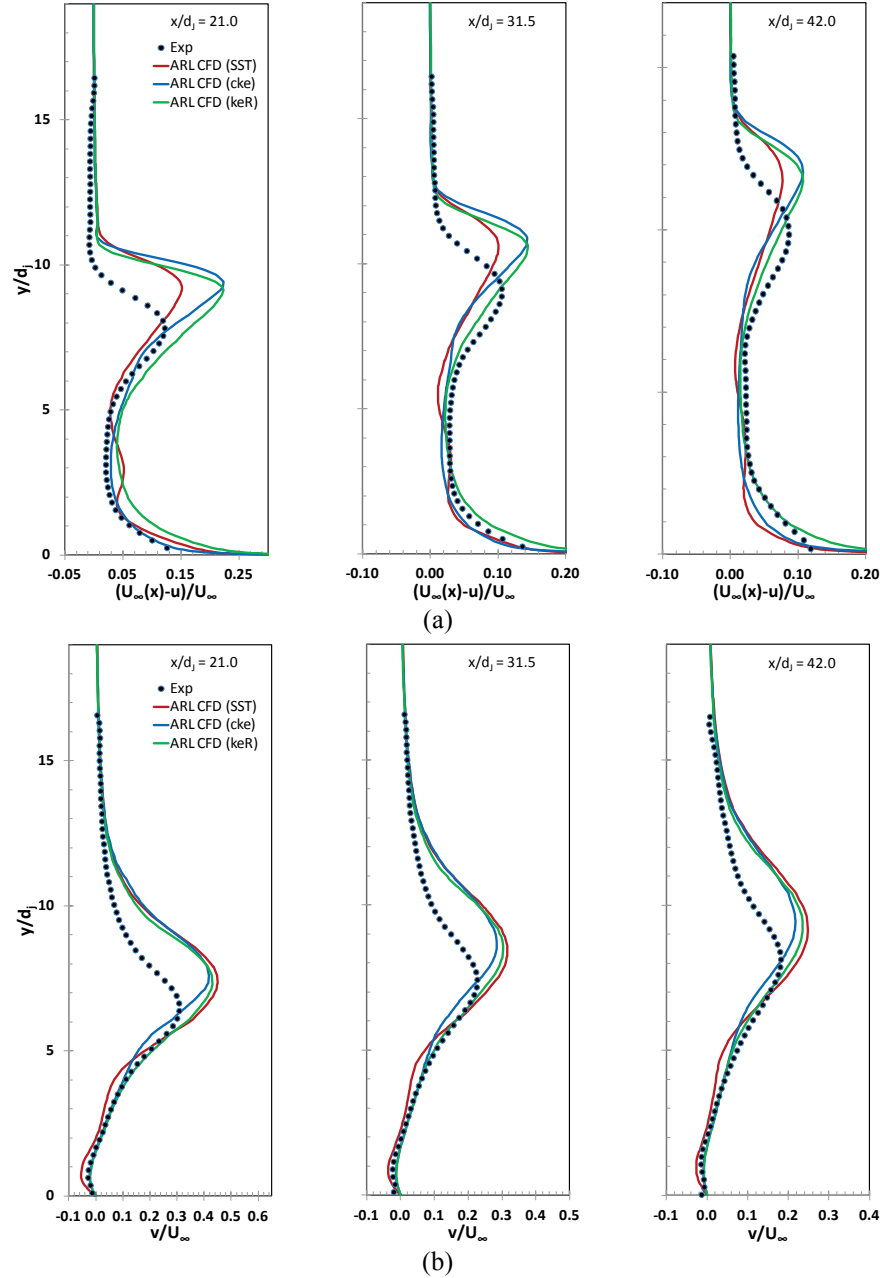
Figure 15. Measured and ARL predicted (a) u-velocity deficit and (b) v-velocity profiles on tunnel centerline at x/d_j = 21.0, 31.5, and 42.0, M_∞ = 0.8, J = 10.2.

The AMRDEC results are shown in terms of percent error between the predicted and measured data (Fig. 16). The location of every PIV data point was compared to the model (interpolated if needed). Figure 16a shows the percent error in the u-velocity between the predicted data and the PIV data. The two black lines on the plot represent the x/d_j = 21.0 and x/d_j = 31.5 locations for the profile plots. The differences in the upper left corner of each plot are due to bad PIV data and should be ignored.[10] The zero percent error has been colored white. It is clear that a majority of the flow is within ±5% error (colors blue and green). The modeled solution penetrated further into

the wind tunnel and, as a result, has a high velocity and this error is shown as the colors yellow and red. This error seems to diminish as the flow moves downstream. Also interesting is the flowfield comparison above the jet plume. The freestream flow is in relative good agreement (~1% error) near the upstream start of the measurements but the model solution tends to become higher in velocity (~5% error) farther downstream. This would indicate that the model solution is causing a greater blockage of the wind tunnel flow as indicated by the greater penetration of the model jet plume.

Since the crossflow v-velocity is near zero in value, the difference between the modeled solution and the PIV measurements—rather than percent error—are shown in Figure 16b. The comparison above and below the jet plume is excellent. The v-velocity comparison shows a peak difference in the jet plume at the upstream start of the comparison and diminishes as the flow moves downstream.

Figure 16c shows the percent error in turbulent kinetic energy (TKE). The large region above the jet is red and represents a 100% error since the modeled solution has a zero value for the TKE but the measured values are positive and non-zero.[6,10] Peak errors within the jet plume reach a high of 300% and indicate that the modeled TKE is much higher in value than the measurements. Below the jet plume, the comparison is reasonable (±50%).

| (a) | (b) | (c) |
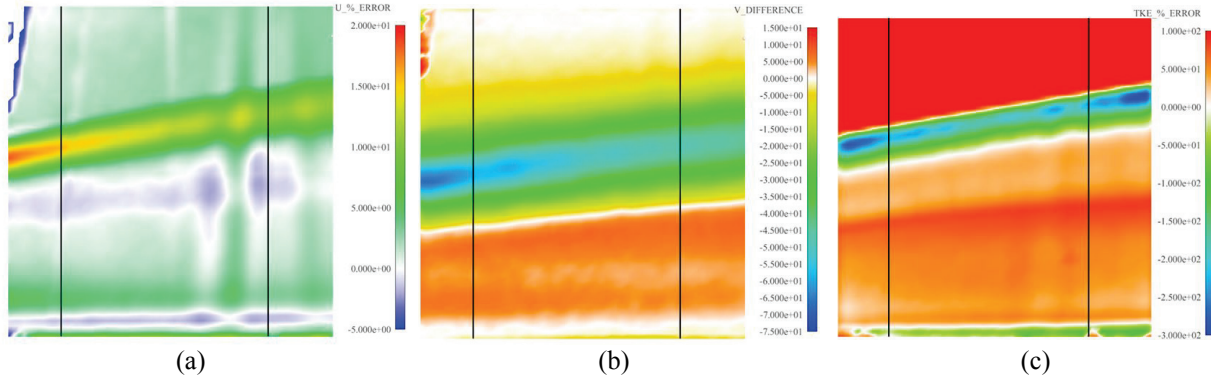
Figure 16. Difference between measured and AMRDEC predicted data: (a) percent error in u-velocity, (b) difference in v-velocity, and (c) percent error in TKE, $M_\infty = 0.8$, $J = 10.2$.

The AMRDEC predicted tunnel centerline u-velocity deficit profiles at locations x/d_j = 21.0, 31.5, and 42.0 downstream of the jet nozzle are shown in Fig. 17. The comparisons are in excellent agreement with the measurements for all locations outside of the jet plume. It is clear from these three plots that the modeled jet plume is broader in width and penetrates further in the y-direction into the tunnel test section. This higher penetration results in a peak error of 16% at 21.0 jet diameters downstream of the jet nozzle and falls to just 9% error at the 42.0 diameters downstream.

The AMRDEC predicted tunnel centerline v-velocity profiles at the same locations downstream of the jet nozzle and are Fig. 18. The v-velocity trends are the same as for the u-velocity profiles. The comparisons between the model flowfield and measurements are in excellent agreement for all locations outside of the jet plume. The core of the computed jet plume is broader and centered higher in the tunnel than shown by the measurements. This difference from measurements decreases as the flow moves downstream.

The AMRDEC predicted tunnel centerline TKE profiles are shown in Fig. 19 for locations of x/d_j = 21.0 and 31.5 (no data was available at x/d_j = 42.0) downstream of the jet nozzle. These two plots clearly show that the modeled jet plume penetrates too high (greater y location) into the tunnel flow when compared with the PIV derived TKE values. The peak values of modeled TKE are similar to the peak measurement derived values but the comparisons, as a percent error, are poor. It is possible that the data collection and post processing of the experimental turbulent stresses may have significant error,[10] and some issues with the data collection and processing were stated.[12]
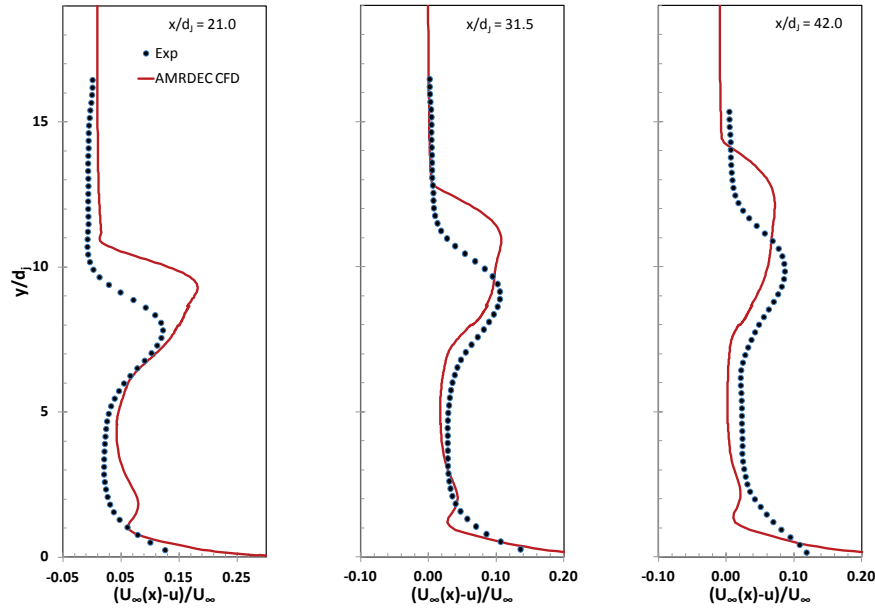
Figure 17. Measured and AMRDEC predicted *u*-velocity deficit profiles on tunnel centerline at *x*/*d_j* = 21.0, 31.5, and 42.0, *M_∞* = 0.8, *J* = 10.2.
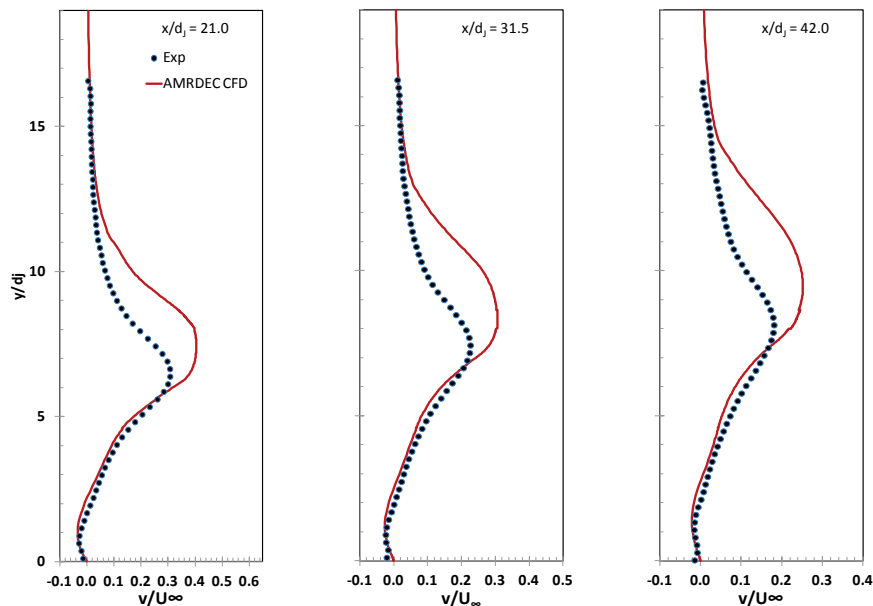

Figure 18. Measured and AMRDEC predicted *v*-velocity profiles on tunnel centerline at *x*/*d_j* = 21.0, 31.5, and 42.0, *M_∞* = 0.8, *J* = 10.2.

The analysis above concentrates on the results from the streamwise PIV measurement plane. However, the lateral extent of the jet interaction flowfield is also important and thus results from the crossflow stereoscopic PIV measurement plane at *x*/*d_j* = 33.8 are now discussed. Figure 20 shows the measured data taken on the crossplane PIV plane for the priority case at *M_∞* = 0.8 and *J* = 10.2. The expected prominent flow features are observed in the measured data such as the kidney bean shape of the jet plume and the Horse-Shoe Vortices (HSV) near the wall caused by the jet plume interaction with the boundary layer.
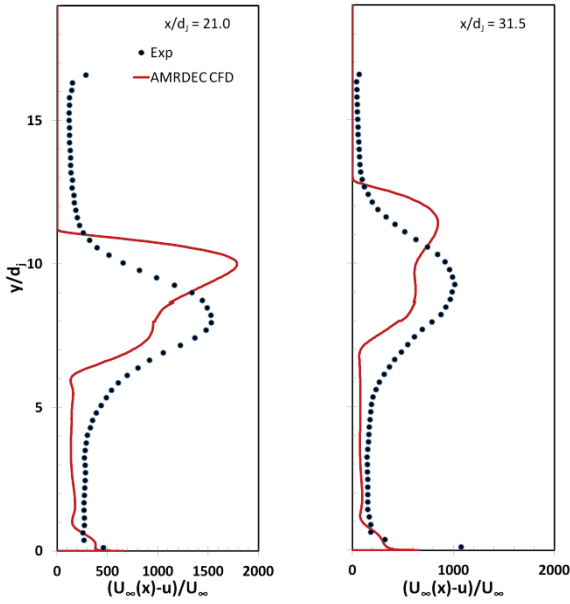
Figure 19. Measured and AMRDEC predicted TKE profiles on tunnel centerline at x/d_j = 21.0 and 31.5, M_∞ = 0.8, J = 10.2.
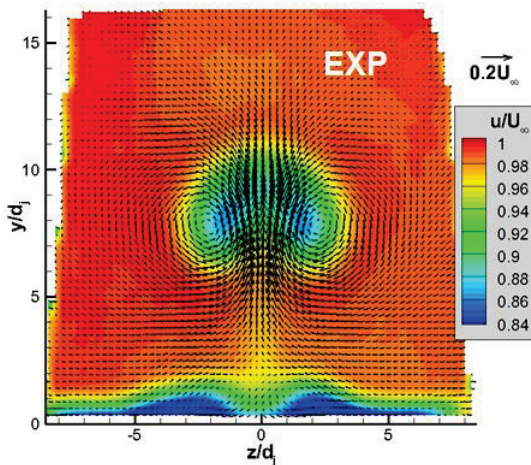
Figure 20.   Experimental u-velocity contours on cross-plane at x/d_j = 33.8, M_∞ = 0.8, J = 10.2 (Beresh et al.[7]).

Figures 21a–d show the DSTL predictions for the four different turbulence models. Note that the computational domain has been mirrored around the X-Z plane of symmetry to make the plots consistent with the measured data in Figure 20. The trajectory of the jet plume is predicted by the SARC model in Fig. 21b to be closer to wall than the experiment, whereas the SA model predicts it to be further away in Fig. 21a. Both the SA and SARC models predict the wake features and the HSV close to the wall fairly well but overpredict the lateral extent of the jet. The location relative to the wall and the strength of the jet plume is overpredicted by both the k-ω and SST models. However, the k-ω and SST models predict the lateral extent of the jet fairly well. Almost no wake features are predicted by either of these turbulence models. Overall, the SA predictions are closest to the measured data at this location.

Figure 22a–c shows the ARL predicted crossflow u-velocity contours for the SST, cke, and keR models, respectively. Again, the predictions from the cke and keR models appear to provide a closer qualitative match to the experimental data (Fig. 20), while the SST model provided the best quantitative match of the streamwise u-velocity profiles (Fig. 15). The data in Fig. 22 have been mirrored about the symmetry plan, as the simulations were performed on one-half the physical domain.
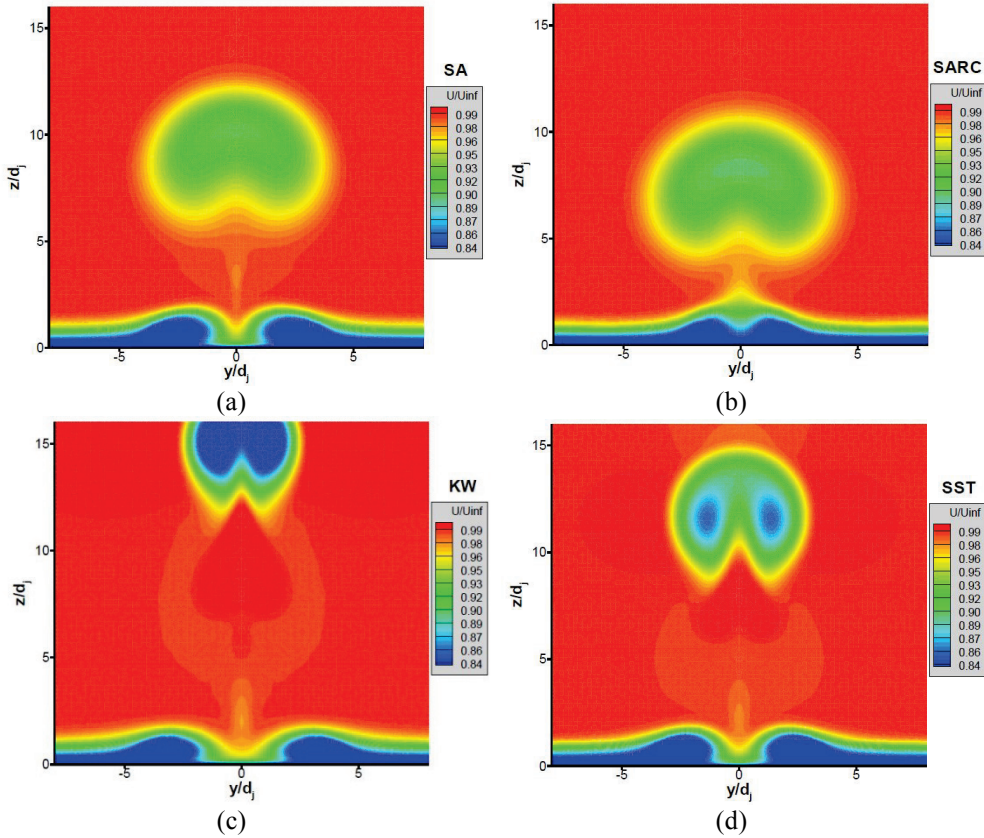
Figure 21. DSTL predicted *u*-velocity contours on cross-plane at *x*/*d*$_j$ = 33.8 using (a) SA, (b) SARC, (c) *k*-*ω*, and (d) *k*-*ω* SST turbulence models, *M*$_∞$ = 0.8, *J* = 10.2.
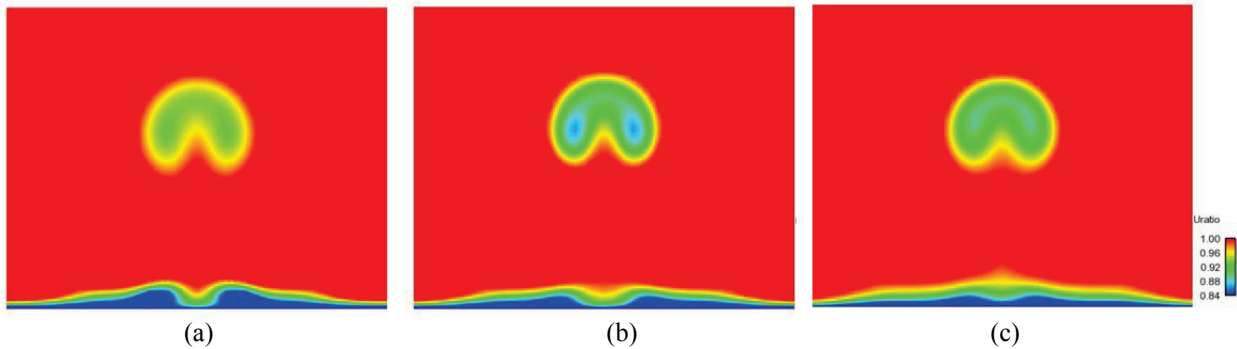

Figure 22. ARL predicted *u*-velocity contours on cross-plane at *x*/*d*$_j$ = 33.8 using (a) SST, (b) cke, (c) keR turbulence models, *M*$_∞$ = 0.8, *J* = 10.2.

Figure 23a shows the AMRDEC predicted *u*-velocity in the lower (inverted) section of the figure, and the experimental data on the same scale in the upper section. The freestream velocity value has been set to the color white. The large thick boundary layer in the lower modeled solution (blue color) is clearly visible on the tunnel walls. For clarity, the *u*-velocity is only plotted over the range from 230 to 290 m/s. The velocity field surrounding the jet in the modeled solution is very constant but counter to the measured values. There is also a large region of lower *u*-velocity above the jet plume in the measurements, and what this feature represents is unknown. The core of the jet appears to be symmetrical in the measurements but asymmetrical in the modeled solution. The modeled solution also appears to 'pull' the boundary layer off to one side, a feature only slightly visible in the PIV data. The percent error in computed *u*-velocity as shown in Fig. 23b shows that the errors in the computed flowfield are within the range of -6 to +18%. If the boundary layer region is ignored, then the *u*-velocity error falls to just ~10%, an excellent comparison.

17

American Institute of Aeronautics and Astronautics

(a)   (b)
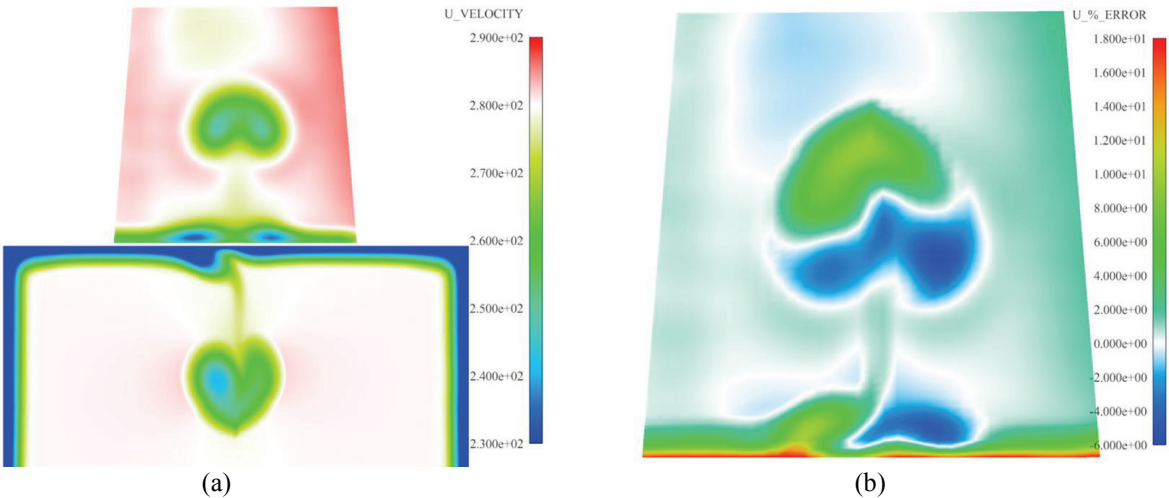
Figure 23. (a) AMRDEC predicted (lower, inverted) and experimental (upper) *u*-velocity contours on cross-plane and (b) percent error in *u*-velocity at x/d_j = 33.8, M_∞ = 0.8, J = 10.2.

The asymmetric HSV-boundary layer interaction was also observed, to a lesser extent, in the ARL computations performed on the full wind tunnel computational domain. Figure 24 compares the mirrored half-domain and full-domain predictions using the SST turbulence model for the priority case shown above. A small asymmetry is observed in the HSV-boundary layer interaction region below the jet plume. No noticeable difference is observed in the jet plume in Fig. 24 and comparison of half- and full-domain velocity profiles showed difference in *u*-velocity only in this region (y/d_j < 4.0).[29] No differences in the *v*-velocity profiles were observed between the half- and full-domain results. To achieve the lower asymmetry in Fig. 24b, many more iterations were run to ensure full convergence of the mass flux thru the tunnel. The half-domain solution appeared converged within about 10000–15000 iterations. The result shown in Fig 24b is after 25000 iterations, though there was little change from that at 20000 iterations.
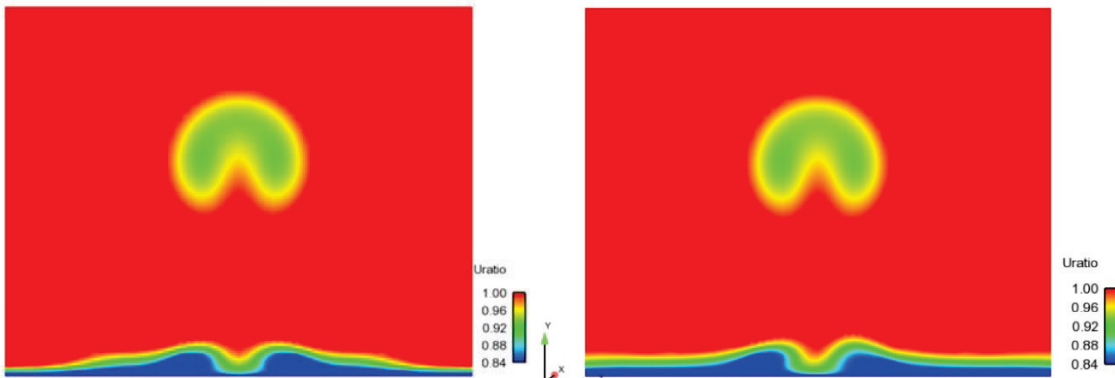
Figure 24. ARL predicted *u*-velocity on cross-plane for (a) mirrored half-domain and (b) full-domain computations using SST turbulence model, M_∞ = 0.8, J = 10.2.

Figures 25 and 26 show comparisons of the *u*-velocity deficit and *v*-velocity profiles, respectively, among the AMRDEC, DSTL, and ARL CFD prediction results. As noted, all three sets of predictions overpredict the penetration of the jet into the tunnel freestream. The DSTL prediction is closest to the experimental data, both in penetration distance and *v*-velocity value, while the ARL prediction is very similar to the DSTL prediction of *u*-velocity deficit. The AMRDEC and ARL predictions are similar in prediction of the *v*-velocity profiles. All three perform reasonably at predicting the region below the jet plume, with some variation in the HSV-boundary layer interaction region.

18
American Institute of Aeronautics and Astronautics
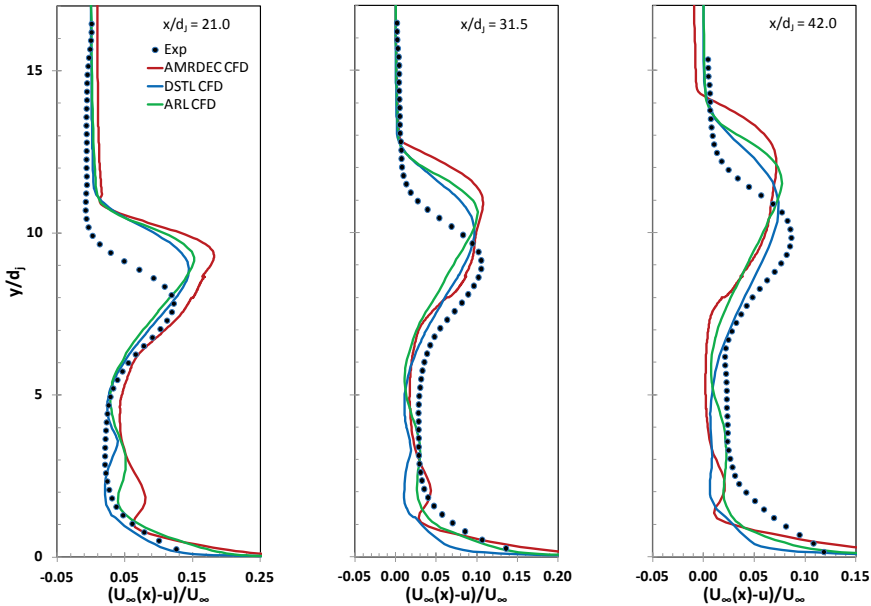
Figure 25. Comparison of AMRDEC (*k-ε*), DSTL (SA), and ARL (SST) predictions with measured *u*-velocity deficit profiles on the tunnel centerline at *x*/*d*_j = 21.0, 31.5, and 42.0, *M*_∞ = 0.8, *J* = 10.2.
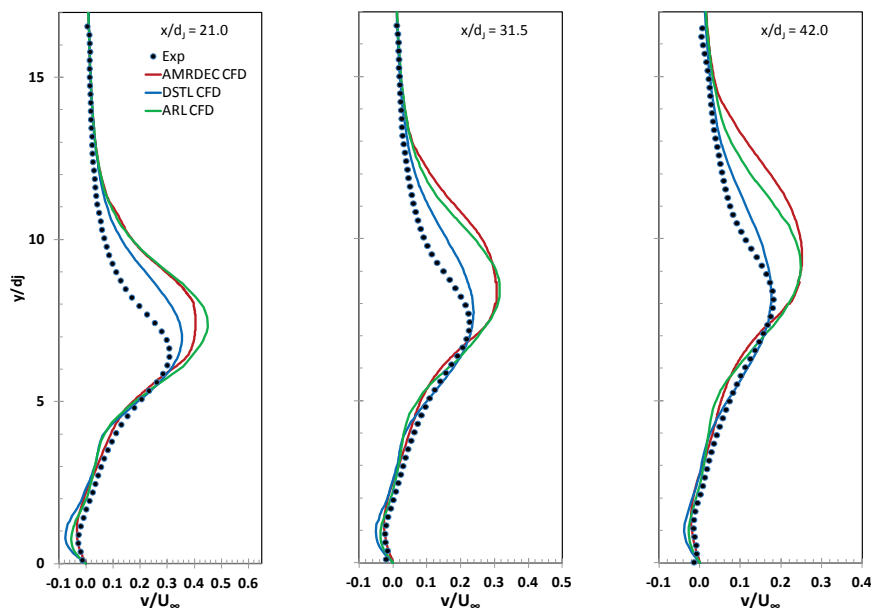

Figure 26. Comparison of AMRDEC (*k-ε*), DSTL (SA), and ARL (SST) predictions with measured *v*-velocity profiles on the tunnel centerline at *x*/*d*_j = 21.0, 31.5, and 42.0, *M*_∞ = 0.8, *J* = 10.2.

In general, the DSTL and ARL predictions of the prominent flow physics were found to be highly sensitive to the turbulence modeling, with different models performing better with different flow solvers. DSTL, using Cobalt, found the SA and SARC models performing better than the k-ω and SST models, with the SA model considered to have performed the best.[11] The ARL results presented here indicate the SST model performed the best in CFD++, based on the quantitative velocity profiles.

Similar prediction results were reported by Arunajatesan[30] for the same experimental test case using the k-ω and SST models and the GASP commercial CFD code. The author found, similar to the present results, that the turbulence models investigated overpredict the velocity deficit in the jet, the strength of the CVP, and failed to capture the location of the vortices. The author also found the predictions of turbulence statistics did not compare

well with the experimental data, as found by AMRDEC.[10] Arunajatesan[30] also performed a detailed analysis of the turbulence modeling assumptions built into the models and concluded that the assumption of common eddy viscosity to relate the turbulent stresses to the strain rate tensor may fail for this flowfield. Arunajatesan and McWherter-Payne[31] later used unsteady, detached-eddy simulations in an attempt to address these deficiencies, but these simulations still were deficient in capturing the overall flow statistics observed in the experiments.

Chai and Mahesh[32] also performed simulations of this same experimental setup using large-eddy simulations. While their predictions of the jet penetration distance compares much better with the experiment, their over prediction of the time-averaged peak u-velocity deficit in the jet plume at $x/d_j = 21.0$ is comparable to those observed in the present study. Chai and Mahesh also predict a little higher u-velocity deficit in the jet wake, $2 \leq x/d_j \leq 5$, than that predicted in the present study. However, Chai and Mahesh's prediction of the peak downstream u-velocity deficit and v-velocity are closer to those observed in the experiment.

2. Effects of pressure ratio

The AMRDEC and DSTL studies included the additional three jet pressure ratios (J = 2.8, 5.6, and 16.7) at Mach 0.8 investigated in the Sandia experiments. This section investigates the capability of CFD to predict the jet interaction flowfield for different jet pressure ratios at a constant freestream Mach number of $M_\infty = 0.8$. All DSTL predictions presented following were performed using the SA turbulence model.

Figure 27a shows the measured u-velocity measurements for the largest jet pressure ratio case of J = 16.7. As expected, a stronger jet plume incurs further into the freestream flowfield than the J = 10.2 case (Fig. 27b). The key flowfield features that include the jet plume and wake flow are very similar to those discussed for the J=10.2 case. The DSTL-predicted flowfield for this case is shown in Fig. 28a. The predicted jet trajectory is further from the wall than the measured data, and this overprediction is consistent with the observations of how the CFD performed in the J = 10.2 case (Fig. 28b). An additional wake flow feature is observed in the computation close to the wall that is not seen in the measured data.
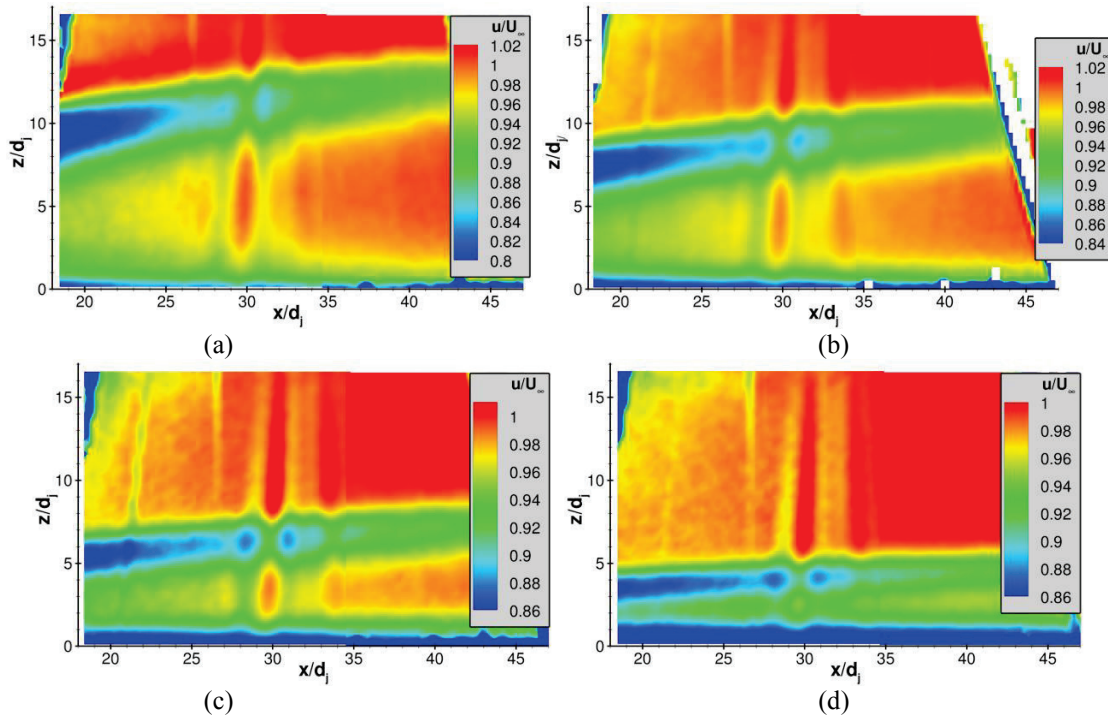

Figure 27. Measured *u*-velocity contours on the tunnel centerline at $M_\infty = 0.8$, J = (a) 16.7, (b) 10.2, (c) 5.6, and (d) 2.8 (Beresh et al.[5]).

At the lower jet pressure ratio of J=5.6 there is good qualitative agreement between the measured data shown in Fig. 27c and the prediction shown in Fig. 28c. In this case, the size and strength of the jet plume are well predicted, as is the jet trajectory. At the lowest jet pressure ratio of J = 2.8, the measured data in Fig. 27d shows a weak but coherent jet that is close to the wall. The predicted flowfield in Fig. 28d does qualitatively show a jet plume,

American Institute of Aeronautics and Astronautics

however there is an additional interaction occurring between the jet and the wall boundary layer that is not observed in the measured data.

Figure 29 shows a quantitative comparison of the measured and DSTL-predicted velocity deficit profiles across the range of jet pressure ratios considered. In general, the CFD captures the trend of the measured data for all jet pressure ratios. The strength of the jet plume and its distance from the top wall, indicated by the maximum velocity deficit, are typically overpredicted in all cases. Generally, there is reasonable quantitative agreement for the prediction of the peak velocity deficit for the jet pressure ratios above $J = 5.6$. At the lowest jet pressure ratio, the predicted velocity distribution between the jet and the wall is roughly constant, indicating a separated flow or wake region. This is a flow feature which is not observed to the same extent in the measured data.

(a)   (b)

(c)   (d)
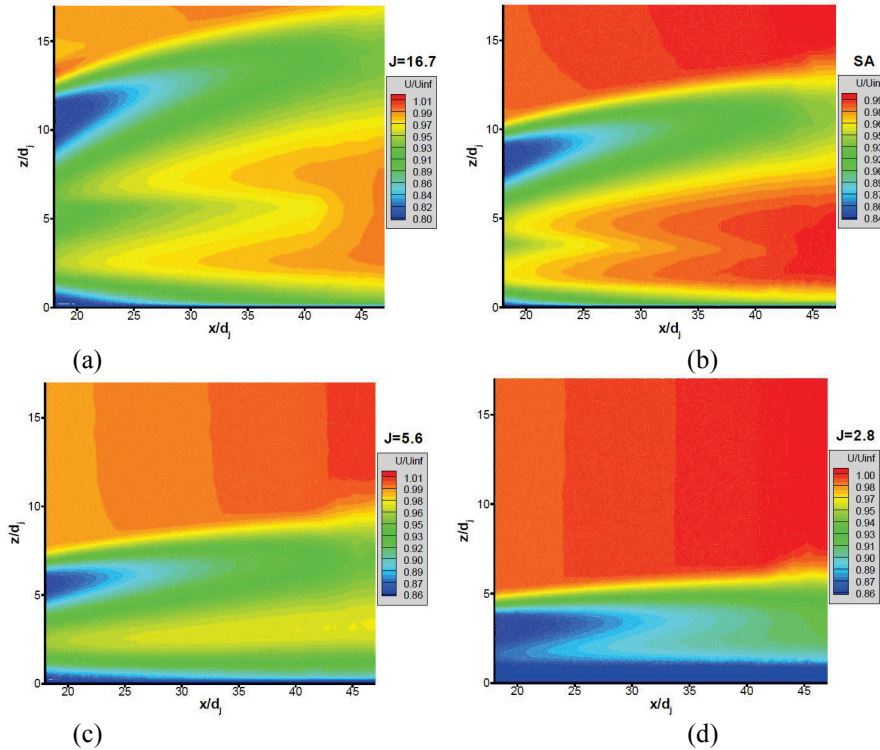
Figure 28. DSTL predicted *u*-velocity contours on tunnel centerline, $M_\infty = 0.8$, J = (a) 16.7, (b) 10.2, (c) 5.6, and (d) 2.8.

The quantitative comparisons of the vertical velocity between the experiment and DSTL predictions are shown in Fig. 30. The agreement is very good over the majority of the flowfield for jet pressure ratios below $J = 10.2$, with accurate prediction of both the vortex strength and location. The predictions are mostly within the experimental uncertainty for most of the velocity profile. At $J = 16.7$, there is an overprediction of the maximum vertical velocity but overall the CFD captures the relevant trend well.

The qualitative comparison of the experimental and AMRDEC-predicted *u*-velocity is shown in Fig. 31, again in the form of percent error between the measured and predicted values. For each case, in the region of the flowfield above the jet plume, the freestream flow is in relative good agreement (~1% error) near the upstream start of the measurements. However, the predicted solution tends to become higher in velocity (~5% error) farther downstream. This indicates that the predicted solution is causing a greater blockage of the wind tunnel flow, as indicated by the greater penetration of the predicted jet plume. For the lower three pressure ratios (Fig. 31b-d) the solution below the jet is in excellent agreement with the data. For the $J = 16.7$ case there appears to be an across-the-board increase in error everywhere with peak values up to 40%. It is speculated that this may be a result of using the same back pressure boundary condition for all four cases. Due to the increased blockage at this higher pressure ratio, the user-set back pressure may need to be adjusted, but there is no data to determine the correct value. For each case, as expected, the jet plume penetrates further into the wind tunnel with increasing pressure, but the predicted plume penetrates further into tunnel than the experimental data indicates. In general, the comparisons to the experimental

American Institute of Aeronautics and Astronautics

data for the axial velocity are in excellent agreement. Similar observations were made for the comparison of the vertical velocity, which were in good agreement to the PIV data.[10]
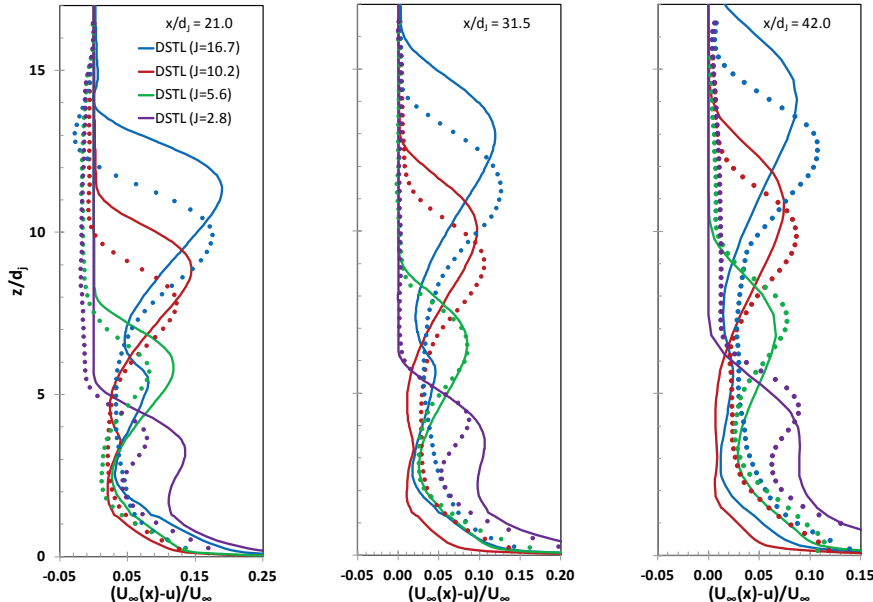

Figure 29. Measured and DSTL predicted u-velocity deficit profiles on the tunnel centerline at x/d_j = 21.0, 31.5, and 42.0, M_∞ = 0.8. (• Experiment, ─ CFD)
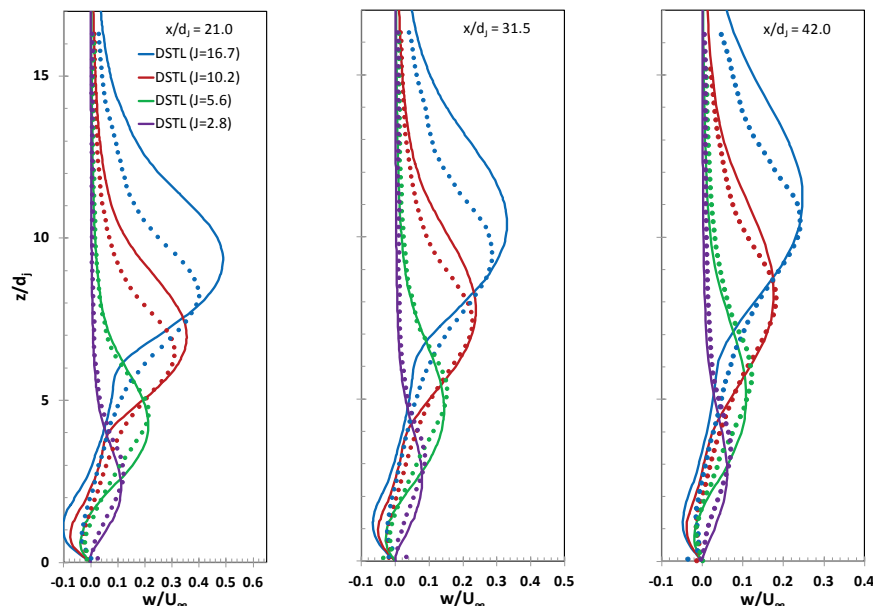

Figure 30. Measured and DSTL predicted w-velocity deficit profiles on the tunnel centerline at x/d_j = 21.0, 31.5, and 42.0, M_∞ = 0.8. (• Experiment, ─ CFD)

The quantitative comparison of the experimental and AMRDEC-predicted u-velocity deficit profiles for each pressure ratio are shown in Fig. 32. In general, all predicted values are in very good agreement with the experimental data for all locations outside of the jet plume. It is clear from the plots that the predicted jet plume is broader in width and penetrates further in the vertical direction for each of the pressure ratios. For the AMRDEC predictions, this higher penetration results in a peak error with the the jet core at x/d_j = 21.0 of 10% for the J = 2.8 case, 13% peak error for the J = 5.6 case, 15% peak error for the J = 10.2 case, and 32% peak error for the J = 16.7 case. The error in each of the four cases dropped significantly (~50%) as the flow moved downstream to the x/d_j =

42.0 location.[10] The trends for the prediction of the *v*-velocity (Fig. 33) profiles are the same, with the core of the predicted jet plume being broader and penetrating further into the wind tunnel.

(a)

(b)

(c)

(d)
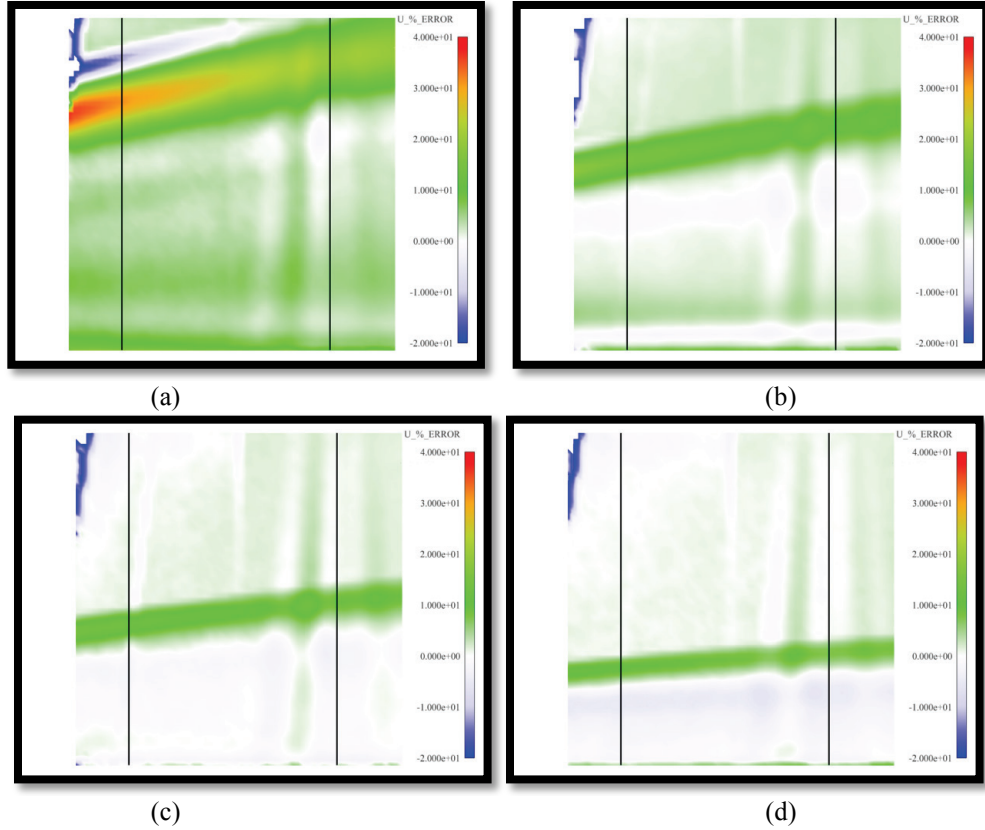
Figure 31. Contours of percent error between experimental and AMRDEC-predicted *u*-velocity on tunnel centerline, $M_\infty = 0.8$, $J =$ (a) 16.7, (b) 10.2, (c) 5.6, and (d) 2.8.
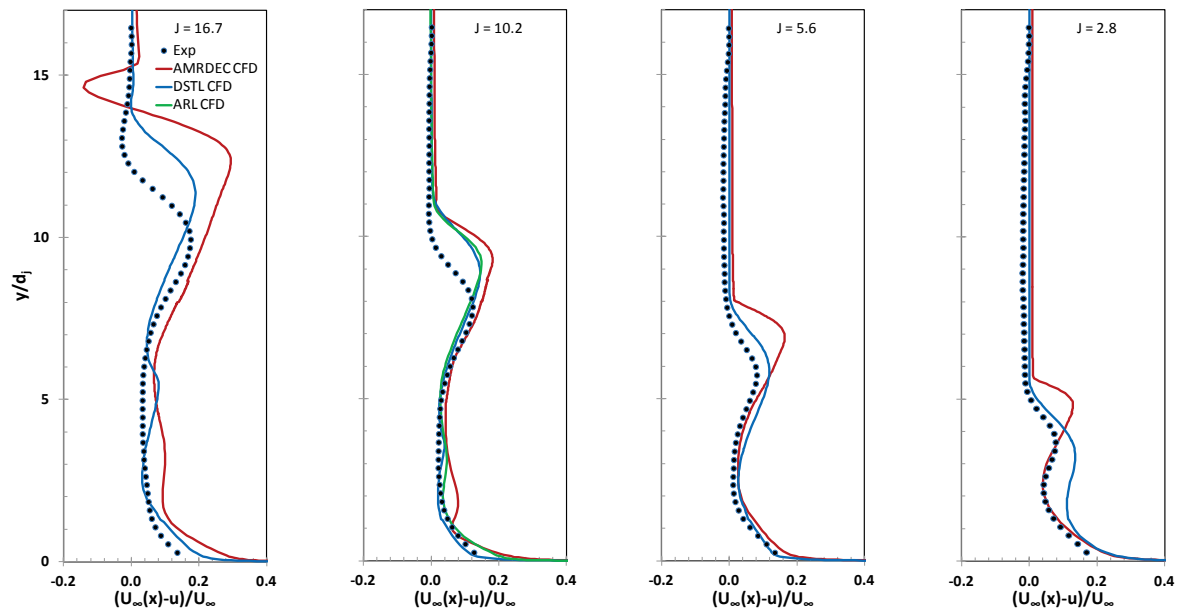

Figure 32. Comparison of AMRDEC (*k*-ε), DSTL (SA), and ARL (SST) predictions with measured *u*-velocity deficit profiles on the tunnel centerline at $x/d_j = 21.0$, $M_\infty = 0.8$, $J = 16.7, 10.2, 5.6$, and 2.8.
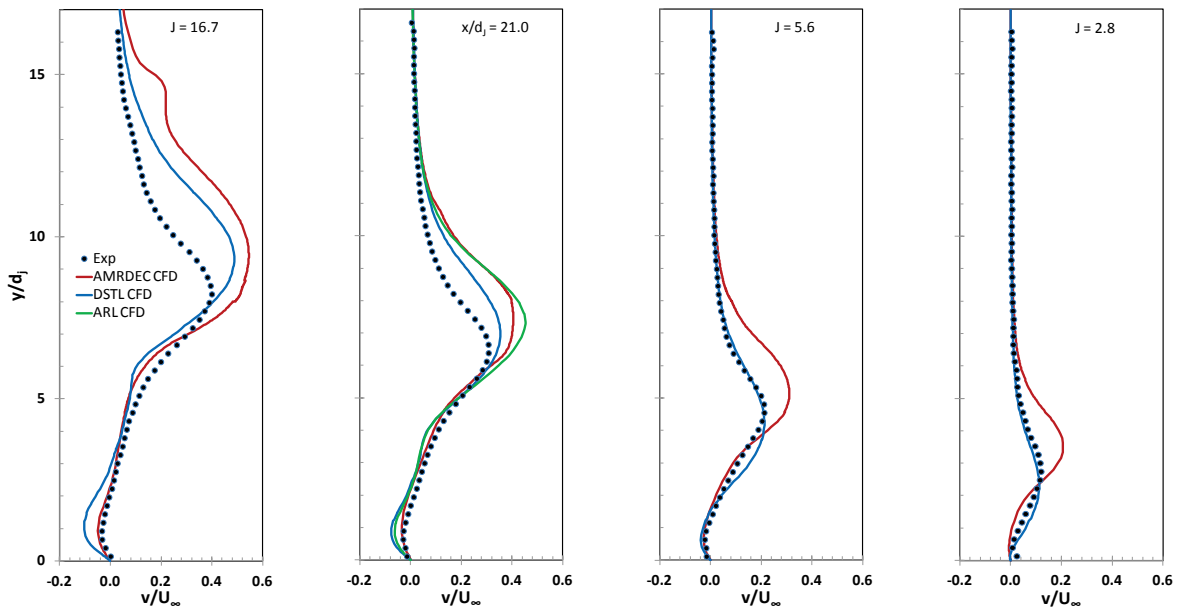
Figure 33. Comparison of AMRDEC (k-ε), DSTL (SA), and ARL (SST) predictions with measured v-velocity profiles on the tunnel centerline at $x/d_j = 21.0$, $M_\infty = 0.8$, $J = 16.7$, 10.2, 5.6, and 2.8.

Figures 32 and 33 also show comparisons of the DSTL-predicted and ARL-predicted ($J = 10.2$ only) velocity profiles to compare the three prediction methods. The closest comparison among the three u-velocity predictions is at $J = 10.2$, where the AMRDEC prediction is only slightly higher in value, but all three predictions agree in the location of the peak u-velocity deficit. At the other three pressure ratios, the AMRDEC solution predicts a slightly larger penetration of the jet plume into the tunnel and larger velocity deficit, except at $J = 2.8$. Similar trends are observed for the v-velocity profiles, shown in Fig. 33.

3. Effects of Mach number

The DSTL study included the effects of Mach number, including the additional Mach numbers of $M_\infty = 0.5$, 0.6, and 0.7. As these results are presented in detail in Ref. 11, they are not repeated here. In summary, the experimental u-velocity flowfield[5] for the $M_\infty = 0.7$ case showed the same qualitative flowfield characteristics as the $M_\infty = 0.8$ case. The experimental data at the $M_\infty = 0.6$ and $M_\infty = 0.5$ cases showed a characteristically different flowfield, possibly indicating that a complex interaction occurs between the jet and the wall boundary layer. In these cases the flow between the jet and the wall does not recover in the same way as observed at the higher Mach numbers.

On the other hand the predicted u-velocity (and v-velocity) for the low-Mach number cases did not agree well with the experimental data at $M_\infty = 0.5$ and $M_\infty = 0.6$. Instead, the interaction flowfield was very similar to that in the higher Mach number cases. The predictions support the rationale that J is a suitable scaling parameter to track the jet and CVP trajectory, as was observed by Beresh et al.[5] at $M_\infty = 0.8$ and $M_\infty = 0.7$. Beresh et al.[5] stated that the failure of the $M_\infty = 0.6$ and $M_\infty = 0.5$ cases to exhibit similarity with the $M_\infty = 0.8$ and $M_\infty = 0.7$ cases was contrary to an earlier experiment in which Schlieren images were acquired of the same interaction.[33] It is stated that those data showed qualitatively similar jet penetration for all four values of M_∞ at $J = 10.2$. It was noted, however, that the nozzle exit diameter was 12.7 mm versus the value of 9.53 mm in the present study, possibly affecting the tendency for separation in the nozzle. However, if the different jet penetration flowfield is due to flow separation in the nozzle, the CFD is still not adequately predicting the effect. Future research should focus on this effect if the low jet-to-freestream pressure ratio regime is of interest.

IV. Summary and Conclusion

The ability of RANS CFD to predict a supersonic lateral jet in a subsonic crossflow has been validated using high fidelity flowfield measurements. The wind tunnel flowfield is well predicted when the jet is turned off and the boundary-layer velocity profiles and wall pressure distributions are in good agreement with the measurements. In

general, the prominent features of the jet interaction flowfield are well captured by all predictions for the jet-on cases. As observed in the experiment, the predicted jet plume and CVP are in different locations and both of these key flow features are found to be highly sensitive to the turbulence model used. In the predictions using the Cobalt solver (DSTL), the one-equation turbulence models (SA, SARC) performed markedly better than the two-equation models and overall, the SA turbulence model performed best. ARL results with the CFD[++] solver indicated the SST turbulence model provided the best overall match with the experimental data. AMRDEC results with the CRAFT solver and the k-ε turbulence model provided comparable results. All three solvers investigate predicted the plume to penetrate further into the crossflow and that the width was greater than observed in the experiment. These results were consistent over the range of jet pressure ratios investigated.

How well these RANS CFD solutions are at predicting these flowfields depends on the level of capability required for the application. If one is attempting to determine detailed aerodynamic force and moment data on a munition with fins or other control surfaces far downstream of the jet nozzle exit (as in the present setup), then it is likely that the predictions will not be adequate. In this case, even small error in the strength and/or location of the CVP or HSV may have significant effect on the induced forces and moments. However, if one needs aerodynamic data for early design development or system performance assessment, then CFD predictions of this level may be adequate. In this case, the CFD predictions will likely still be better than anything acquired with an engineering level model, since the CFD will provide an estimate of the jet amplification factors and subsequent effective jet location.[34–36]

In addition, if the jet nozzle exit is located close to any control surfaces with which interaction may occur (e.g., near or within a set of tail fins), then the CFD prediction of the aerodynamic forces and moments may be adequate. Unfortunately, no experimental data was available in the jet near-field in the present study. However, other research has shown excellent results in predicting the jet near-field surface pressure profiles (in a supersonic crossflow),[3,37] a possible indication of improved prediction of near-field jet plume characteristics.

Acknowledgments

References

[1]Dowdy, M. W., and Newton, J. F., "Investigation of Liquid and Gaseous Secondary Injection Phenomena on a Flat Plate with M = 2.01 and M = 4.54." JPL-TR-32-542, Dec. 1963.

[2]Kovar, A., and Schulein, E., "Comparison of experimental and numerical investigation on a jet in a supersonic cross-flow," *The Aeronautical Journal*, Vol. 110, pp. 353–360, June 2006.

[3]Gnemmi, P., and Schafer, H. J., "Experimental and Numerical Investigations of a Transverse Jet Interaction on a Missile Body," AIAA-2005-0052, January 2005

[4]Seiler, F., Gnemmi, P., Ende, H., Schwenzer, M., and Meuer, R., "Jet interaction at supersonic cross flow conditions," *Schock Waves*, Vol. 13, No. 1, pp. 13–23, 2003.

[5]Beresh, S. J., Henfling, J. F., Erven, R. J., and Spillers, R. W., "Penetration of a Transverse Supersonic Jet into a Subsonic Compressible Crossflow," *AIAA Journal*, Vol. 43, No. 2, 2005, pp. 379–389 (also presented as paper AIAA-2004-1112).

[6]Beresh, S. J., Henfling, J. F., Erven, R. J., and Spillers, R. W., "Turbulent Characteristics of a Transverse Supersonic Jet into a Subsonic Compressible Crossflow," *AIAA Journal*, Vol. 43, No. 11, 2005, pp. 2385–2394 (also presented as paper AIAA-2004-2341).

[7]Beresh, S. J., Henfling, J. F., Erven, R. J., and Spillers, R. W., "Crossplane Velocimetry of a Transverse Supersonic Jet in a Transonic Crossflow," *AIAA Journal*, Vol. 44, No. 12, 2006, pp. 3051–3061 (also presented as paper AIAA-2006-0906).

[8]Beresh, S. J., Henfling, J. F., Spillers, R. W., and Erven, R. J., "Measurement of Experimental Boundary Conditions for CFD Validation of a Supersonic Jet in Transonic Crossflow," AIAA-2006-3449, June 2006.

[9]Technical Cooperation Program, URL: http://www.acq.osd.mil/ttcp/ [cited 4 November 2013]

[10]Kennedy, K. D., and Mikkelsen, C. D., "Part II: RANS Computational Fluid Dynamics Comparisons to a Supersonic Jet in Subsonic Crossflow," Proceedings of the JANNAF 45th Combustion, 33rd Airbreathing Propulsion, 33rd Exhaust Plume & Signatures, 27 Propulsion Systems Hazards Joint Subcommittee Meeting, Naval Postgraduate School, Monterey, CA Dec 3-7, 2012.

[11]Chaplin, R. A., "RANS CFD Predictions of a Supersonic Jet in a Transonic Crossflow," AIAA-2013-2911, June 2013.

[12]Beresh, S. J., "Comparison of PIV data using multiple configurations and processing techniques," *Exp Fluids*, Vol. 47, pp. 883–896, 2009.

[13]Pointwise, Inc., GRIDGEN version 15.17 User Manual, 2011.

[14]So, R. M. C. Zhang, H. S., and Speziale, C. G., "Near-Wall Modeling of the Dissipation Rate Equation," *AIAA Journal*, Vol. 29, No. 12, 1991, pp. 2069–2076.

[15]Sinha, N., Hosangadi, A. and Dash, S.M., "The CRAFT NS code and Preliminary Applications to Steady/Unsteady, Reacting, Multi-Phase Jet/Plume Flowfield Problems," JANNAF 19th Exhaust Plume Technology Meeting, CPIA Pub. 568, May 1991, pp. 203–226.

[16]Kennedy, K. D., Mikkelsen, C. D., and Walker, B. J., "RANS Calculations and Comparisons To Data For An Axisymmetric Wake Flow," JANNAF 29th Exhaust Plume Technology Subcommittee Meeting, CPIA Pub. JSC CD-44, 2B-10-Kennedy, 19-23 June 2006, Littleton, Colorado.

[17]Hosangadi, A. Lee, R. A., York, B. J., Sinha, N., and Dash, S. M., "Upwind Unstructured Scheme for Three-Dimensional Combusting Flow," *Journal of Propulsion and Power*, Vol. 12, No. 3, May-June 1996, pp. 494–503.

[18]Cobalt LLC, "Cobalt user's manual," 2007.

[19]Strang, W., Tomaro, R., and Grismer, M., "The defining methods of Cobalt60: A parallel, implicit, unstructured Euler/Navier–Stokes solver," AIAA Paper 1999-0786, 1999.

[20]Spalart, P. R., and Allmaras, S. R., "A One-Equation Turbulence Model for Aerodynamic Flows," AIAA-92-0439, Januray 1992.

[21]Shur, M. L., Strelets, M. K., Travin, A. K., Spalart, P. R., "Turbulence Modeling in Rotating and Curved Channels: Assessing the Spalart-Shur Correction," *AIAA Journal*, Vol. 38, No. 5, 2000, pp. 784–792.

[22]Wilcox, D., "Turbulence Modeling for CFD," 3rd Edition, DCW Industries, La Canada, CA, 2006.

[23]Menter, F. R., "Two-Equation Eddy-Viscosity Turbulence Models For Engineering Applications," *AIAA Journal*, Vol 32, No. 8, 1994, pp. 1598–1605.

[24]Suzen, Y. B., and Hoffmann, K. A., "Investigation of Supersonic Jet Exhaust Flow by One- and Two-Equation Turbulence Models," AIAA-98-0322, January 1998.

[25]Metacomp Technologies, Inc., "MIME User Manual," Agoura Hills, CA, 2008.

[26]Metacomp Technologies, Inc., "CFD++ Users Manual," Agoura Hills, CA, 2011.

[27]Goldberg U, Batten, P, Palaniswamy, S, Chakravarthy, S, Peroomian, O, "Hypersonic Flow Predictions Using Linear and Nonlinear Turbulence Closures," *AIAA Journal of Aircraft* Vol. 37, No. 4, 2000, pp. 671–675.

[28]Goldberg U, Peroomian, O, Chakravarthy, S, "Application Of The k-ε-R Turbulence Model To Wall-Bounded Compressive Flows," AIAA 98-0323, January 1998.

[29]DeSpirito, J., "CFD Validation Investigation of a Supersonic Jet in a Subsonic Crossflow," ARL report in preparation.

[30]Arunajatesan, S., "Evaluation of Two-Equation RANS Models for Simulation of Jet-in-Crossflow Problems," AIAA-2012-1199, January, 2012.

[31]Arunajatesan, S., and McWherter-Payne, M. A., "Unsteady Modeling of Jet-in-Crossflow Problems," AIAA-2013-3099, June 2013.

[32]Chai, X., and Mahesh, K., "Simulations of High Speed Turbulent Jets in Crossflows," AIAA-2011-0650, January 2011.

[33]Beresh, S. J., Henfling, J. F., and Erven, R. J., "Flow Separation Inside a Supersonic Nozzle Exhausting into a Subsonic Compressible Crossflw, "*Journal of Propulsion and Power*, Vol. 19, No. 4, 2003, pp. 655–662 (also presented as paper AIAA-2002-1067).

[34]DeSpirito, J., "Factors Affecting Reaction Jet Interaction Effects on Projectiles," AIAA-2011-3031, June 2011.

[35]DeSpirito, J., "Lateral Jet Interaction on a Finned Projectile in Supersonic Flow," AIAA-2012-0413, January 2012.

[36]DeSpirito, J., "Lateral Reaction Jet Flow Interaction Effects on a Generic Fin-Stabilized Munition in Supersonic Crossflows," ARL Technical Report ARL-TR-6707, Aberdeen Proving Ground, MD, November 2013.

[37]DeSpirito, J., "Turbulence Model Effects on Cold-Gas Lateral Jet Interaction in a Supersonic Crossflow," AIAA-2014-3023, June 2014.